Title

Value of Quantitative Susceptibility Mapping in Clinical Neuroradiology

Abstract

Quantitative susceptibility mapping (QSM) is a unique technique for providing quantitative information on tissue magnetic susceptibility using phase image data. QSM can provide valuable information regarding physiological and pathological processes such as iron deposition, hemorrhage, calcification, and myelin. QSM has been considered for use as an imaging biomarker to investigate physiological status and pathological changes. Although various studies have investigated the clinical applications of QSM, particularly regarding the use of QSM in clinical practice, have not been examined well. This review provides on an overview of the basics of QSM and its clinical applications in neuroradiology.

Key words

quantitative susceptibility mapping; magnetic resonance imaging; computed tomography; neuroradiology

Background

Susceptibility weighted imaging (SWI) has been widely used in clinical practice for the evaluation of various both abnormalities and normal structures in the brain (1). SWI is created by multiple multiplications of the high-pass-filtered phase image with the magnitude image. Although 2D T2*-weighted gradient recalled echo (GRE) imaging is still used in clinical practice, more susceptibility information can be obtained from SWI with its 3D high resolution GRE imaging without partial volume effect (1). T2* mapping or R2* mapping (R2*= 1/ T2*) calculated from multiple echo GRE sequence has been used for the measurement of susceptibility. Both T2* and R2* mapping provide useful contrast reflecting tissue microstructures, but magnetic susceptibility has been difficult to characterize on T2* or R2* mapping (1,2).

With the development of quantitative susceptibility mapping (QSM), the spatial susceptibility distribution can be visualized by measuring local field shifts in tissues (3-5). Both phase and magnitude images are required to create QSM as mentioned later. Iron, myelin and calcification are the major sources of tissue susceptibility in the brain, and QSM can differentiate between paramagnetic (e.g., iron) and diamagnetic (e.g., myelin, calcification) substances. Tissue susceptibility values can also be determined using QSM.

Although various studies of QSM have been conducted, the clinical applications

of QSM, particularly regarding the use of QSM in clinical practice, have not been examined well. Since QSM provides unique information on susceptibility, the use of QSM in daily clinical practice and clinical research has potential to enhance the value of QSM in radiology. It is important for both radiologists and QSM developers to know how QSM can be useful in clinical practice. This review article provides an overview of the basics of QSM and the resulting clinical applications, particularly in terms of recent works in neuroradiology.

Procedures

In most cases, magnitude and phase images of GRE are used to create QSM. Reconstruction of QSM requires the following steps: 1) creating a brain mask; 2) phase unwrapping; 3) background field removal; and 4) solving an ill-posed inverse problem. Various approaches have been proposed for each step, so only a brief introduction is given here; please refer to previous articles if more detailed information is required (2,6-9).

1) Creating a brain mask: A binary mask image is required to determine the region of interest for processing phase images. Magnitude images are used to generate brain masks, then skull stripping such as with Brain Extraction Tool (BET) in FSL (https://fsl.fmrib.ox.ac.uk/fsl), or other thresholding algorithms are used (10).

2) Phase unwrapping: Since phase values can be shown only within a range of -π and π, phase aliasing may occur if the phase exceeds the bounds of |π|. The details are described in previous papers (2,6-9). Various techniques have been proposed for phase unwrapping, such as using path-based methods in the spatial domain and linear fitting methods in the temporal domain, to obtain an estimate of true magnetic field perturbation (11,12).

3) Background phase removal: Background phase removal, which separates the tissue phase and background phase arising outside the tissue, is important to obtain a tissue phase to determine tissue magnetic susceptibility. Many algorithms have been proposed and representative ones include sophisticated harmonic artifact reduction for phase data (SHARP) (13); regularization enabled SHARP (RESHARP) (14); harmonic background phase removal using the Laplacian operator (HARPARELLA) (15); and projection onto dipole fields (PDF) (16).

4) Solving the ill-posed inverse problem: To determine tissue susceptibility, deconvolution of the tissue field with the dipole kernel is necessary. Deconvolution in image space is division in k-space, and the dipole kernel is zero when an observation point relative to the dipole source is at ± 54.7º (magic angle) with respect to the B0 direction (7). These zeroes result in an ill-posed inverse problem to obtain tissue susceptibility, and many algorithms have been proposed to solve this problem (13,17,18).

5) Software: Many QSM software packages are currently available and representative toolboxes are listed (https://github.com/mathieuboudreau/qsm-tools#tools). Open data including the 2016 QSM reconstruction challenge is also available (19).

Deep learning (DL) methods

DL has recently been applied to QSM reconstruction. In most DL QSM pipelines, the network is trained using data obtained from Calculation Of Susceptibility through Multiple Orientation Sampling (COSMOS) or traditional optimization techniques performed on measured MR data, and as the input data of the measured MR data (20). DL has been developed for each step of QSM reconstruction, and despite high expectations, several intrinsic issues remain in DL QSM (20). When test data possess different characteristics to the training data, such as test data from a patient with hemorrhage and training data from healthy subjects, unexpected errors may arise (20). Further work is expected to improve the problems associated with DL QSM.

Image sequences for QSM

The GRE sequence is often used for QSM, since the phase image of GRE reflects local magnetic field changes. Optimal phase contrast is achieved for echo time (TE) equal

to the effective transverse relaxation time T2* of the tissue (21). Since tissues with different T2* values exist, multiple echo GRE sequence is desirable for QSM. Single echo GRE with Wave-CAIPI acquisition has been used in cases with limited scan time, such as COSMOS acquisition requiring scans in multiple orientations (22). In addition, 3D echo planar imaging (EPI) with a single TE is also used for QSM with a faster scan time (23,24). QSM can now also be created on-line from 3 TE image sequences of STrategically Acquired Gradient Echo (STAGE) imaging (25).

QSM across different magnetic fields

The phase of a voxel is generally assumed to linearly follow the main magnetic field and acquisition TE (4). Several factors may affect the results of QSM, including susceptibility anisotropy associated with subject positioning, and acquisition parameters including coverage, spatial resolution, and TE (26,27). QSM has demonstrated good-to-excellent reproducibility at both 3 T and 1.5 T (28,29).

Brain MRI at 7 T is beneficial due to the excellent contrast-to-noise ratio, and the benefits of QSM at 7 T have been reported (30). A study comparing 7 T and 3 T showed that QSM at 7 T offered excellent image quality with good reproducibility (31). Acceptable reproducibility was also achieved between 7 T and 3 T with minimal

underestimation of susceptibility at 7 T (31). Notably, optimal reproducibility was obtained when TEs at 3 T was ~2.6 times longer than those at 7 T, suggesting that different TEs should be selected for different field strengths (26).

Magnetic susceptibility source separation

QSM shows the susceptibility of the voxel, but does not characterize the sub-voxel susceptibility distribution. In physiological tissues, both paramagnetic and diamagnetic susceptibility sources may exist within a certain voxel. The opposite susceptibility components may cancellate each other inside the voxel, and the ability to separate opposing susceptibility sources at the sub-voxel level has been anticipated to evaluate the specific quantification of the magnetic properties of a tissue, particularly where iron is deposited inside white matter.

A previous attempt at separating opposing magnetic sources was performed by assuming that both $R2^*$, and bulk susceptibility χ depend linearly on the concentration of iron, concentration of myelin, and a constant (32). The recent approach, χ-separation, is based on the hypothesis that R2' and frequency shift are determined by susceptibility concentration in the static dephasing regime (33). R2 and $R2^*$ measurements are used to obtain R2' map (33). Another approach, DECOMPOSE-QSM algorithm, utilizes a 3-pool

signal model where each voxel comprises three distributed pools of magnetic sources: paramagnetic; diamagnetic; and magnetically "neutral" (34). Multi-echo GRE data is used in this model (34). In- and ex-vivo studies has been performed for these new techniques and excellent separation has been achieved, but further studies may be needed to validate the models.

The role of QSM in clinical practice

Paramagnetic substances such as iron appear positive on QSM, while diamagnetic substances such as calcification and myelin are shown as negative susceptibility. Since both paramagnetic and diamagnetic substances are shown as low signals on SWI, differentiation between paramagnetic and diamagnetic susceptibility with QSM may facilitate a clinical understanding of signal intensity on SWI. QSM can be used for evaluating iron content in association with both normal aging and abnormal iron deposition, whereas CT cannot provide useful information. Anatomical landmarks such as deep gray matter regions, optic radiations, and physiological calcification of the pineal gland and choroid plexus are easily recognized on QSM. With better delineation of the subthalamic nuclei on QSM, QSM is useful for accurate placement of electrodes during deep brain stimulation surgery (35). Susceptibility values derived from QSM can be used

for serial evaluations and group comparisons.

Presumably normal QSM findings

In brain QSM of normal subjects, most human tissues are diamagnetic, with susceptibility values are shown within ±20% of the susceptibility value of water (36). The deep gray matter, including parts of the cortices, and veins show positive susceptibility in normal subjects due to iron (ferritin) deposition, and deoxyhemoglobin, respectively. White matter structures show slightly negative susceptibility due to myelin, with the optic radiation and internal capsules showing negative susceptibility. Although iron is present in oligodendrocytes, the diamagnetic property of abundant myelin is thought to be a major factor in the susceptibility of white matter (5,37). Physiological calcification of the pineal body and choroid plexus frequently shows as obvious negative susceptibility.

Age and sex-related differences in QSM

Iron is paramagnetic substance and the major source of positive susceptibility in the brain. Although stored iron is minimal in neonates, iron concentration in the deep gray matter and cortical areas increase with age, with a particularly rapid increase from birth until about 20 years of age (Fig. 1) (2,38). QSM likewise demonstrates similar age-related

changes in susceptibility (39-42). Susceptibility in the motor cortices increases throughout life. While the susceptibility of iron-rich deep gray matter also increases, the time courses differ. The susceptibility of the globus pallidus plateaus after 20-30 years, while those of the putamen and caudate nuclei continue to increase into the 80s (39).

Myelin is diamagnetic and causes negative susceptibility. White matter fiber bundles and subcortical white matter exhibit a consistent biphasic temporal pattern with an initial decrease followed by an increase in susceptibility, potentially representing the maturation and later breakdown of myelin (39). Temporal characteristics, especially the time to reach minimum susceptibility, vary among different white matter fiber bundles.

Sex differences in susceptibility have been reported for deep gray matter structures, with women showing lower levels of susceptibility in the substantia nigra after accounting for age (40). Women expected to be post menopause show lower total magnetic susceptibility in the subcortical brain than younger female subjects or male subjects of any age (40).

Paradoxical calcification or mineralization

CT shows high attenuation in regions with calcification such as the choroid plexus and pineal body, and QSM shows negative susceptibility values in those regions

because calcification is diamagnetic. However, CT occasionally shows high attenuation, particularly in the medial part of the globus pallidus, and QSM shows positive susceptibility in the corresponding regions (paradoxical calcification) (Fig. 2). This finding was evaluated histopathologically, demonstrating the presence of iron and calcification at the vascular wall of the globus pallidus (43). This may be because calcification at the vascular wall shows high attenuation on CT, and positive susceptibility in relation to iron overwhelms the negative susceptibility associated with calcification on QSM (44). Meanwhile, paramagnetic substances such as iron shows a lesser effect on CT attenuation (44). Similar phenomena are encountered in Fahr disease, and discussed later. Magnetic source separation technique, which can estimate both paramagnetic and diamagnetic susceptibility, may help provide biophysical information in areas of paradoxical calcification (33,34).

Microbleeds

Pathologically, old cerebral microbleeds are hemosiderin deposits caused by minor extravasation of blood from small, fibrohyalinized arterioles (45). Microbleeds are frequently detected in patients with hypertension (24) and are better visualized at 3 T compared to lower magnetic field strengths. QSM is reportedly to be useful in evaluating

microbleeds with better contrast than magnitude images from SWI (46).

Cerebral amyloid angiopathy (CAA)

CAA is characterized by the deposition of β amyloid in the walls of small to medium sized arteries (47). The pathogenesis remains uncertain but seems likely to involve locally produced amyloid accumulates in the brain and accumulates as a result of reduced clearance. CAA is associated with intracranial hemorrhage (ICH) and CAA-associated ICH tends to be multifocal, and recurrent, with lobar location (47). CAA occasionally accompanies encephalopathy as so-called as CAA-related inflammation, presenting with acute or subacute onset of headaches, cognitive and behavioral changes, seizures and focal neurological deficits. Perivascular or intramural vascular inflammation and deposition of amyloid in blood vessels in the cerebral cortex and leptomeninges are observed histopathologically (47).

Multiple microbleeds tend to be observed at gray-white matter junction, but can also appear in the superficial cerebellum in CAA. Microbleeds are less commonly observed in the basal ganglia and brainstem. Subarachnoid hemorrhage or superficial siderosis is occasionally observed in adjacent sulci.

In CAA-related inflammation, patchy or confluent, asymmetrical white matter

hyperintensities are observed on T2WI and FLAIR (Fig. 3). Contrast enhancement is seen in the leptomeninges or parenchymal lesions. SWI shows multiple microhemorrhages, sometimes accompanied by subcortical hemorrhage, which QSM shows as high susceptibility legions (Fig. 3).

Moyamoya disease

Moyamoya disease is characterized by progressive stenosis involving the terminal internal carotid arteries with small collateral vessels. Abnormal vascular networks that develop around the stenotic lesions, may work as collateral pathways. Hemorrhage is one of the severe complications of moyamoya disease and follow-up detection of microbleeds may be effective for predicting future hemorrhage (48). Disruption of the dilated collateral vessels due to hemodynamic stress or rupture of peripheral aneurysms that form in collateral vessels are possible sources of such bleeding (Fig. 4) (49).

Although SWI is better than T2*-weighted imaging to detect microbleeds (50), QSM is effective for detecting microbleeds due to the conspicuity of such lesions, and the ability to differentiate hemosiderin from calcification.

Neurodegenerative diseases

The presence of iron is essential for normal brain function and development, but excessive iron deposition has been proposed as critical to various pathophysiologies of the brain. QSM allows for quantitative estimation of tissue magnetic susceptibility at the voxel level, through the differentiation between paramagnetic and diamagnetic substances. Since iron content is not directly measured by QSM, the pathophysiologies of different neurodegenerative diseases must be carefully considered when interpreting tissue susceptibility information. QSM has been applied for various neurodegenerative diseases.

a) Parkinson's disease (PD)

PD is characterized by degeneration and atrophy of the dopaminergic neurons in the substantia nigra along with intracellular deposition of α-synuclein. Neuromelanin-sensitive MR revealed that neuromelanin loss in the substantia nigra is associated with degrees of motor deficits especially in the advanced stage of PD (51-53). Increased QSM values in the substantia nigra have been found in PD patients compared to controls, and these values correlate with the severity of motor disability in PD (54). Increased iron content in the substantia nigra does not necessarily represent dopaminergic neurodegeneration in the substantia nigra, however. Striatal dopaminergic denervation on

dopamine transporter single photon emission computed tomography (SPECT) followed by abnormal iron accumulation in the substantia nigra on QSM has been shown to precede the neuromelanin loss associated with dopaminergic neuronal loss (55).

b) Neurodegeneration with brain iron accumulation (NBIA)

Ceruloplasmin is the extracellular iron transporter and plays an important role in minimizing intracellular levels of ferrous iron. Aceruloplasminemia is a severe adult-onset NBIA in which iron accumulates within perivascular astrocytes due to insufficient efflux cellular iron. QSM shows elevated ferrihydrite-iron as the source of iron-sensitive MR (56).

QSM shows increased susceptibility in the globus pallidus and substantia nigra compared to controls in panthothenate kinase-associated neurodegeneration (PKAN), one of the NBIA syndromes (57). In mitochondrial membrane protein-associated neurodegeneration (MPAN), another syndrome of NBIA, significantly higher susceptibility has been found in the substantia nigra, globus pallidus, and caudate nucleus compared to findings from healthy controls (58).

c) Amyotrophic lateral sclerosis (ALS)

ALS is a progressive neurodegenerative disease characterized by the degeneration of motor neurons in the brain and spinal cord. The clinical presentation of

ALS is heterogeneous in respect to the motor neurons involved, but the symptom typically begins in the limbs. Atrophy and reduced thickness of the motor cortex is commonly observed. Impaired iron homeostasis in the brain has been associated with oxidative damage, eventually manifesting as neuronal cell degeneration (59).

Although decreased signal intensity is noted on SWI in patients with ALS, QSM shows higher detection of abnormalities associated with high levels of iron in the motor cortex (60). QSM demonstrated that magnetic susceptibility in the precentral cortex reflected the prevalence of upper or lower motor neuron predominant ALS (61). Increased tissue iron loading was identified on QSM not only in the motor cortices, but also in the substantia nigra, globus pallidus, red nucleus, and putamen (62). However, whether iron accumulation is a cause or consequence of the neuropathological changes in ALS remains unclear (59).

d) Cerebellar ataxia

Iron accumulation in the dentate nucleus is a well-known finding in healthy aging and various NBIAs. Occasionally, unexpectedly decreased susceptibility values are seen in the dentate nucleus in neurodegenerative disease. Cerebellar atrophy and low susceptibility values in the dentate nucleus offer a clue to suspicion of abnormal gliosis in spinocerebellar ataxia type 6 (SCA6) (63,64). Conversely, QSM also reveals a marked

elevation of susceptibility in SCA1 and multiple system atrophy-cerebellar subtype (MSA-C), moderate elevation in Friedreich ataxia, and a tendency toward elevated susceptibility in SCA2, to be compared to unaltered susceptibility in SCA3 (64). Microglial activation has been reported in SCA1 and MSA-C (65), so iron accumulation accompanying microglia has been suspected. Iron-rich microglia may be less pronounced in SCA2 and SCA3 than in SCA1 (64). SCA6 typically manifests as a relatively pure cerebellar phenotype and is thought to be caused primarily by degeneration of Purkinje cells in the cerebellar cortex (66). Loss of neurons possibly due to trans-synaptic degeneration, and reactive astrogliosis have been reported in the cerebellar nuclei of SCA6 patients (64).

Cerebral autosomal dominant arteriopathy with subcortical infarcts and leukoencephalopathy (CADASIL)

CADASIL is a hereditary cerebral small vessel disease associated with the NOTCH3 gene. The NOTCH3 extracellular domain accumulates in arterial walls followed by degeneration of vascular smooth muscle cells, and subsequent fibrosis and stenosis of the arterioles, predominantly in the cerebral white matter (67). Clinical symptoms include migraine with aura, ischemic attacks, cognitive decline and dementia,

and psychiatric manifestations.

Hyperintensity on FLAIR in the temporopolar regions and external capsules are characteristic MR findings of CADASIL. Widespread injury to the white matter tract, including demyelination and axonal injury, is commonly observed, and QSM revealed increased iron deposition in the caudate and putamen that correlates with the extent of white matter tract injury (68).

Amyloid deposition

Amyloid deposition and neurofibrillary tangles co-localize with neuronal iron accumulation, and Alzheimer disease (AD) pathology and more specifically amyloid deposition it has been demonstrated to be indirectly reflected by the phase information from a T2*-weighted MR sequence (69). QSM showed correlations between iron deposition and amyloid accumulation based on amyloid positron emission tomography (PET) (70,71). In addition, ferritin levels in cerebrospinal fluid (CSF) appear independently related to cognitive performance (72). Patients with AD onset at an early age have a greater neocortical iron burden than late-onset patients (73), thus so QSM is expected to play an important role in evaluating early AD (74).

Idiopathic basal ganglia calcification (IBGC)

IBGC, also called Fahr disease, is a rare, inherited or sporadic neurodegenerative disorder showing calcification in bilateral basal ganglia and dentate nuclei (75). Symptoms of IBGC are clinically heterogeneous and the condition may be asymptomatic or present with movement disorders. Diagnosis is based on neuroimaging in the absence of other explanations for calcification. Calcifications are present as areas of high attenuation on CT, and histology shows calcium deposits in the walls of arterioles and small veins and along capillaries (75). Conversely, QSM shows negative susceptibility representing calcification as well as positive susceptibility suggesting iron accumulation. Various metallic compounds (e.g., zinc, iron, copper, manganese, and aluminum) are deposited in calcified areas, and the strong paramagnetic property of iron presumably overwhelms the susceptibility of other sources (Fig. 5) (44).

When localized temporal or temporofrontal lobe atrophy as well as calcification of symmetrical basal ganglia mimicking Fahr disease are observed, the result should be noted as diffuse neurofibrillary tangles with calcification (DNTC) (76). Although symptoms of IBGC may include dementia, DNTC can be differentiated from IBGC due to the presence of progressive dementia, localized lobar atrophy and tau pathology (76).

Wernicke encephalopathy

The pathophysiology of Wernicke encephalopathy is thought to involve cytotoxic and vasogenic edema due to dysfunctions of the Krebs cycle and pentose phosphate pathway. High intensity lesions on FLAIR may appear in bilateral periventricular regions of the thalamus, hypothalamus, and periaqueductal regions. SWI detects petechial hemorrhages in the mammillary bodies (77). Contrast enhancement in the mammillary bodies, an important imaging sign of Wernicke encephalopathy, suggests a disrupted blood-brain barrier, which may be the cause of the microbleeds. Hemosiderin deposition in bilateral mammillary bodies can be demonstrated on QSM for patients with Wernicke encephalopathy (Fig. 6) (78).

Hepatic encephalopathy

High concentrations of ammonia can cross the blood-brain barrier, where astrocytic glutamine synthetase converts ammonia and glutamate into glutamine, which then acts as an osmolyte and increases cerebral volume (79). While ammonia is the root cause of hepatic encephalopathy, another possible contributor to hepatic encephalopathy is manganese toxicity, particularly against a background of longstanding hepatic cirrhosis. Manganese accumulation and deposition in Alzheimer type II astrocytes in the globus

pallidus are currently considered the main underlying cause of motor disorders associated with acquired hepatocerebral degeneration (80). QSM showed elevated susceptibility values in the globus pallidus, since manganese is a paramagnetic substance (Fig. 7).

Brain tumors

Calcification is seen in various brain tumors, including oligodendroglioma, pilocytic astrocytoma, dysembryoplastic neuroepithelial tumor, medulloblastoma, ependymoma, ganglioglioma, choroid plexus papilloma (carcinoma), craniopharyngioma, central neurocytoma, meningioma, and metastatic tumors especially from mucinous colon adenocarcinoma (81). The incidence of calcification varies with each tumor. Identifying the presence of calcification may help narrow the differential diagnosis, differentiating between neoplastic calcification and intratumoral hemorrhage. Although a description of susceptibility characteristics for all the different types of brain tumors is beyond the scope of this review, we will discuss the commonly encountered entities of glioma, germinoma, and meningioma.

a) Glioma

High-grade gliomas such as glioblastoma and metastatic brain tumors are often associated with hemorrhage. Detection of an intra-tumoral susceptibility signal (ITSS) on

SWI is important because the ITSS grade on SWI has been associated with the size of postoperative hemorrhage after stereotactic biopsy (82).

Among gliomas, calcification is most commonly observed in oligodendroglioma, but is rare in astrocytic neoplasm, including glioblastoma. Oligodendroglial tumors is associated with calcifications such as nodular or clumped patterns. Other brain tumors such as dysembryoplastic neuroepithelial tumor, medulloblastoma, gangliocytoma, and pineoblastoma may also present with calcification.

Representative cases of glioma with QSM are shown in Figures 8, 9, and 10.

b) Germinoma

Primary central nervous system (CNS) germ cell tumors are more common in Japan and other countries in Asia compared with North America, and germinoma is the most common subtype of germ cell tumor. Germinoma tends to occur in the midline, most commonly in the pineal region (Fig. 11) and hypothalamus, and occasionally in the basal ganglia, thalamus, brainstem, and spinal cord. Germinomas are primarily tumors of young patients, with most patients being under than 20 years old at the time of diagnosis (83). Germinoma in the pineal region shows a marked male preponderance, whereas that in the suprasellar region shows no clear gender preponderance.

Germinoma in the pineal regions shows ovoid or lobulated in contours, engulfing

the calcified pineal gland (84). In pineal parenchymal tumors, calcification of the pineal gland may be “exploded”.

c) Meningioma

Meningioma is a common intracranial tumor arising from arachnoid cap cells. Most meningiomas grow slowly or remain stable in size. Meningiomas are occasionally accompanied by calcified components. Meningioma without calcification is likely to grow exponentially, whereas meningioma with calcification shows linear or no growth (85).

When a tumor contains a calcified component, SWI shows low intensity and QSM shows a negative susceptibility value. If the tumor is located along the dura mater, QSM can differentiate positive susceptibility structures suggesting venous structures from negative susceptibility structures suggestive of calcification.

Calcifying pseudoneoplasms of the neuraxis (CAPNON)

CAPNON is a non-neoplastic, calcified lesion occurring anywhere in the CNS (86) (Fig. 12). CAPNON lesions are reportedly intra- or extra-axial, or in the brain or spine (86). No predilections for sex, age, or CNS location have been reported (86). Although the nature of CAPNON is unclear, a reactive rather than a hamartomatous

process has been favored.

Treatment-related intratumoral calcification

Chemotherapeutic agents such as bevacizumab (a vascular endothelial growth factor inhibitor) can also cause calcification within the tumor as a therapeutic effect. QSM can help distinguish between intratumoral hemorrhage and treatment-responsive intratumoral calcification (87). Bevacizumab-induced tumor calcifications in patients with glioblastoma were reported to be related to better outcomes and QSM may provide such supplementary information instead of CT, since CT is not accepted as a sufficient standard of care to evaluate the status of brain tumors in patients.

Radiation-induced mineralizing microangiopathy

Treatment-induced calcifications have only been recognized as rather long-term sequelae of radiotherapy, typically for childhood tumors, such as medulloblastoma. Mineralizing microangiopathy was detected in 30% of childhood brain tumor survivors who underwent radiotherapy at a median 20 years after radiotherapy cessation (88). Mineralizing microangiopathy is diagnosed after identifying calcifications characteristic of mineralizing microangiopathy on QSM or CT.

Arteriovenous fistula (AVF)

In dural AVF, curvilinear subcortical calcifications can be seen on CT in patients with long-standing cortical venous reflux, possibly due to chronic venous congestion (89,90). The exact mechanisms underlying the subcortical calcification of dural AVFs are unknown, but are proposed to represent an arterial steal phenomenon or persistent venous congestion, with calcification occurring in chronic hypoperfused brain parenchyma or secondary to dystrophic changes in the walls of congested veins (Fig 13) (89,90). Cerebral subcortical white matter regions are located in watershed areas of the arterial supply, and are more sensitive to hypoxic or ischemia changes. Arterial venous malformation may also contain dystrophic calcifications along the serpentine vessels and within adjacent parenchyma (89,90).

Cavernous malformation

Cavernous malformation, also known as cavernous angioma, is a common hemorrhagic vascular anomaly comprising clusters of dilated sinusoidal channels lined with endothelial cells (91). Cavernous malformation is grossly distinct from the adjacent brain and has a lobulated appearance. Blood products of various ages are often observed

in cavernous malformation, and developmental venous anomalies or calcifications (so-called popcorn-ball calcification) may occasionally be present. QSM has been reported as useful to monitor the progression of cavernous malformation based on its ability to measure iron content inside the lesion (92).

Infections

QSM may play a certain role in the evaluation of infectious disease.

a) Tuberculoma

Intracranial tuberculosis can affect the meninges and parenchyma, resulting in diffuse meningitis, tuberculoma, tuberculous abscess, focal cerebritis, vasculitis and strokes. Tuberculoma and tuberculous meningoencephalitis are the important manifestations of tuberculosis of the CNS. Tuberculomas are well-defined focal masses that result from tuberculosis infection, and most commonly occur in the brain. The target sign, as a small focus of calcification or enhancement in the center of a ring-enhancing mass, may be present in some cases. Tuberculomas can also mimic other entities, including glioblastoma, brain metastasis, intracranial hemorrhage, abscesses, or other gliomas, which can be associated with calcifications that produce the “target sign” that suggests reactivated or dormant tuberculosis (93). QSM helps distinguish between

calcification and hemosiderin, both of which present as hypointensity signal on SWI (Fig. 14).

b) Toxoplasma

Neurotoxoplasmosis is a common opportunistic infection, that often presents with multiple lesions in the basal ganglia, thalamus, and corticomedullary junctions. A ring-enhancing lesion with a small eccentric nodule along the wall is known as an eccentric target sign. Intralesional susceptibility signal foci are present in the vast majority of patients with neurotoxoplasmosis (94). Calcifications are observed once treatment is initiated (Fig. 15). Calcifications are also observed in cases with congenital toxoplasmosis.

Metallic deposition associated with exogenous sources

QSM can be used for metallic deposition associated with exogenous sources.

a) Gadolinium deposition

Hyperintensity signal in the dentate nucleus and globus pallidus on T1WI is assumed to be a consequence of the number of previous administrations of gadolinium-based contrast agents (GBCA) (95,96). Gadolinium shows paramagnetic properties and magnetic susceptibility on QSM is associated with the number of usages of linear-type GBCA since free gadolinium may accumulate in the dentate nucleus (97). Currently,

macrocyclic GBCA is usually used for contrast-enhanced (CE) MRI due to better chemical stability. Recent reports have noted that even the use of macrocyclic GBCA is associated with increased susceptibility values in the globus pallidus (98). The mechanism has not been clearly determined, but in vivo competition between endogenous cations and gadolinium ions may be considered one reason (99).

b) Transfusion

One unit of packed red blood cells contains approximately 200–250 mg of iron (100), and with approximately 10–20 consecutive transfusions, iron is deposited in tissues where toxicity may result. Comparisons between transfusion-dependent and non-transfusion-dependent beta-thalassemia patients and healthy controls showed disease-related increases in iron content in the putamen and choroid plexus (101). This increase was accentuated by regular blood transfusions (102).

Outside the brain

QSM has also been applied to the regions outside the brain (103). Applications of QSM are currently limited, but future progress is expected.

a) Carotid artery

Carotid plaque with characteristics of intraplaque hemorrhage, lipid-rich

necrosis and calcification may increase the risk of stroke. Vessel wall MRI is widely used to detect hyperintensity inside the plaque, representing intraplaque hemorrhage (104).

QSM has the potential to differentiate intraplaque properties using susceptibility information (105,106). Susceptibility values are higher in intraplaque hemorrhage than in lipid-rich necrosis, and lower in intraplaque calcification than in lipid-rich necrosis (105,106). The reproducibility of susceptibility values inside the carotid plaque have also been demonstrated (105). In addition, susceptibility values are reportedly sensitive to the microstructural composition of arterial vessels, especially for collagen. QSM can provide a sensitive and specific marker of vessel disease by detecting disruption of the microstructures of the carotid arterial wall (107).

b) Liver

Hepatic iron overload is observed as a complication of hemochromatosis, transfusional hemosiderosis and non-alcoholic fatty liver disease (108,109). Measuring hepatic iron content is important to guide iron removal therapy and avoid disease progression (110). Respiratory motions, presence of fat, and severe iron overload complicate QSM in the abdomen, but clinical hepatic iron content can be assessed by using QSM through various techniques (108,109).

c) Prostate

Multiparametric MR imaging including high resolution T2WI, DWI, and dynamic contrast imaging, offers a useful technique for detecting of prostatic cancer (111). However, multiparametric MR imaging can be confounded by post-biopsy hemorrhage and/or calcification. Both CT and QSM allow quantitative differentiation of calcification from non-calcified prostate tissue, and a significant correlation between values from CT and QSM has been observed for calcification (112). Since QSM can accurately depict prostatic calcifications, QSM can be used as an additive tool for multiparametric MR imaging.

Conclusions

We have provided a review of the background and clinical applications of QSM on the basis of the published evidence. Quantitative susceptibility values as well as qualitative information for paramagnetic and diamagnetic properties contribute valuable etiological and diagnostic information. The addition of QSM to routine protocols would increase the clinical utility of MRI.

References

1. Haacke EM, Xu Y, Cheng YC, Reichenbach JR. Susceptibility weighted imaging (SWI). Magn Reson Med 2004;52(3):612-618.

2. Deistung A, Schweser F, Reichenbach JR. Overview of quantitative susceptibility mapping. NMR Biomed 2017;30(4).

3. de Rochefort L, Brown R, Prince MR, Wang Y. Quantitative MR susceptibility mapping using piece-wise constant regularized inversion of the magnetic field. Magn Reson Med 2008;60(4):1003-1009.

4. Wharton S, Schafer A, Bowtell R. Susceptibility mapping in the human brain using threshold-based k-space division. Magn Reson Med 2010;63(5):1292-1304.

5. Li W, Wu B, Liu C. Quantitative susceptibility mapping of human brain reflects spatial variation in tissue composition. Neuroimage 2011;55(4):1645-1656.

6. Haacke EM, Liu S, Buch S, Zheng W, Wu D, Ye Y. Quantitative susceptibility mapping: current status and future directions. Magn Reson Imaging 2015;33(1):1-25.

7. Wang Y, Spincemaille P, Liu Z, et al. Clinical quantitative susceptibility mapping (QSM): Biometal imaging and its emerging roles in patient care. J Magn Reson Imaging 2017;46(4):951-971.

8. Vinayagamani S, Sheelakumari R, Sabarish S, et al. Quantitative Susceptibility

Mapping: Technical Considerations and Clinical Applications in Neuroimaging. J Magn Reson Imaging 2021;53(1):23-37.

9. Liu C, Li W, Tong KA, Yeom KW, Kuzminski S. Susceptibility-weighted imaging and quantitative susceptibility mapping in the brain. J Magn Reson Imaging 2015;42(1):23-41.

10. Smith SM. Fast robust automated brain extraction. Hum Brain Mapp 2002;17(3):143-155.

11. Abdul-Rahman HS, Gdeisat MA, Burton DR, Lalor MJ, Lilley F, Moore CJ. Fast and robust three-dimensional best path phase unwrapping algorithm. Appl Opt 2007;46(26):6623-6635.

12. Jenkinson M. Fast, automated, N-dimensional phase-unwrapping algorithm. Magn Reson Med 2003;49(1):193-197.

13. Schweser F, Deistung A, Lehr BW, Reichenbach JR. Quantitative imaging of intrinsic magnetic tissue properties using MRI signal phase: an approach to in vivo brain iron metabolism? Neuroimage 2011;54(4):2789-2807.

14. Sun H, Wilman AH. Background field removal using spherical mean value filtering and Tikhonov regularization. Magn Reson Med 2014;71(3):1151-1157.

15. Li W, Avram AV, Wu B, Xiao X, Liu C. Integrated Laplacian-based phase

unwrapping and background phase removal for quantitative susceptibility mapping. NMR Biomed 2014;27(2):219-227.

16. de Rochefort L, Liu T, Kressler B, et al. Quantitative susceptibility map reconstruction from MR phase data using bayesian regularization: validation and application to brain imaging. Magn Reson Med 2010;63(1):194-206.

17. Schweser F, Deistung A, Lehr BW, Reichenbach JR. Differentiation between diamagnetic and paramagnetic cerebral lesions based on magnetic susceptibility mapping. Med Phys 2010;37(10):5165-5178.

18. Liu J, Liu T, de Rochefort L, et al. Morphology enabled dipole inversion for quantitative susceptibility mapping using structural consistency between the magnitude image and the susceptibility map. Neuroimage 2012;59(3):2560-2568.

19. Langkammer C, Schweser F, Shmueli K, et al. Quantitative susceptibility mapping: Report from the 2016 reconstruction challenge. Magn Reson Med 2018;79(3):1661-1673.

20. Jung W, Bollmann S, Lee J. Overview of quantitative susceptibility mapping using deep learning: Current status, challenges and opportunities. NMR Biomed 2022;35(4):e4292.

21. Duyn JH, van Gelderen P, Li TQ, de Zwart JA, Koretsky AP, Fukunaga M. High-

field MRI of brain cortical substructure based on signal phase. Proc Natl Acad Sci U S A 2007;104(28):11796-11801.

22. Bilgic B, Xie L, Dibb R, et al. Rapid multi-orientation quantitative susceptibility mapping. Neuroimage 2016;125:1131-1141.

23. Langkammer C, Bredies K, Poser BA, et al. Fast quantitative susceptibility mapping using 3D EPI and total generalized variation. Neuroimage 2015;111:622-630.

24. Wicaksono KP, Fushimi Y, Nakajima S, et al. Two-Minute Quantitative Susceptibility Mapping From Three-Dimensional Echo-Planar Imaging: Accuracy, Reliability, and Detection Performance in Patients With Cerebral Microbleeds. Invest Radiol 2021;56(2):69-77.

25. Haacke EM, Chen Y, Utriainen D, et al. STrategically Acquired Gradient Echo (STAGE) imaging, part III: Technical advances and clinical applications of a rapid multi-contrast multi-parametric brain imaging method. Magn Reson Imaging 2020;65:15-26.

26. Lancione M, Donatelli G, Cecchi P, Cosottini M, Tosetti M, Costagli M. Echo-time dependency of quantitative susceptibility mapping reproducibility at different magnetic field strengths. Neuroimage 2019;197:557-564.

27. Liu C. Susceptibility tensor imaging. Magn Reson Med 2010;63(6):1471-1477.

28. Hinoda T, Fushimi Y, Okada T, et al. Quantitative Susceptibility Mapping at 3 T and 1.5 T: Evaluation of Consistency and Reproducibility. Invest Radiol 2015;50(8):522-530.

29. Deh K, Nguyen TD, Eskreis-Winkler S, et al. Reproducibility of quantitative susceptibility mapping in the brain at two field strengths from two vendors. J Magn Reson Imaging 2015;42(6):1592-1600.

30. Okada T, Fujimoto K, Fushimi Y, et al. Neuroimaging at 7 Tesla: a pictorial narrative review. Quant Imaging Med Surg 2022;12(6):3406-3435.

31. Spincemaille P, Anderson J, Wu G, et al. Quantitative Susceptibility Mapping: MRI at 7T versus 3T. J Neuroimaging 2020;30(1):65-75.

32. Schweser F, Deistung A, Lehr BW, Sommer K, Reichenbach JR. SEMI-TWInS: simultaneous extraction of myelin and iron using a T2*-weighted imaging sequence. Proceedings of the 19th Meeting of the International Society for Magnetic Resonance in Medicine; 2011. p. 120.

33. Shin HG, Lee J, Yun YH, et al. chi-separation: Magnetic susceptibility source separation toward iron and myelin mapping in the brain. Neuroimage 2021;240:118371.

34. Chen J, Gong NJ, Chaim KT, Otaduy MCG, Liu C. Decompose quantitative susceptibility mapping (QSM) to sub-voxel diamagnetic and paramagnetic components based on gradient-echo MRI data. Neuroimage 2021;242:118477.

35. Dimov AV, Gupta A, Kopell BH, Wang Y. High-resolution QSM for functional and structural depiction of subthalamic nuclei in DBS presurgical mapping. J Neurosurg 2018;131(2):360-367.

36. Schenck JF. The role of magnetic susceptibility in magnetic resonance imaging: MRI magnetic compatibility of the first and second kinds. Med Phys 1996;23(6):815-850.

37. Todorich B, Pasquini JM, Garcia CI, Paez PM, Connor JR. Oligodendrocytes and myelination: the role of iron. Glia 2009;57(5):467-478.

38. Harada T, Kudo K, Fujima N, et al. Quantitative Susceptibility Mapping: Basic Methods and Clinical Applications. Radiographics 2022;42(4):1161-1176.

39. Li W, Wu B, Batrachenko A, et al. Differential developmental trajectories of magnetic susceptibility in human brain gray and white matter over the lifespan. Hum Brain Mapp 2014;35(6):2698-2713.

40. Persson N, Wu J, Zhang Q, et al. Age and sex related differences in subcortical brain iron concentrations among healthy adults. Neuroimage 2015;122:385-398.

41. Zhang Y, Shi J, Wei H, Han V, Zhu WZ, Liu C. Neonate and infant brain development from birth to 2 years assessed using MRI-based quantitative susceptibility mapping. Neuroimage 2019;185:349-360.

42. Otani S, Fushimi Y, Iwanaga K, et al. Evaluation of deep gray matter for early brain development using quantitative susceptibility mapping. Eur Radiol 2023;33(6):4488-4499.

43. Kim H, Jang J, Kang J, et al. Clinical Implications of Focal Mineral Deposition in the Globus Pallidus on CT and Quantitative Susceptibility Mapping of MRI. Korean J Radiol 2022;23(7):742-751.

44. Oshima S, Fushimi Y, Okada T, et al. Brain MRI with Quantitative Susceptibility Mapping: Relationship to CT Attenuation Values. Radiology 2020;294(3):600-609.

45. Fazekas F, Kleinert R, Roob G, et al. Histopathologic analysis of foci of signal loss on gradient-echo T2*-weighted MR images in patients with spontaneous intracerebral hemorrhage: evidence of microangiopathy-related microbleeds. AJNR Am J Neuroradiol 1999;20(4):637-642.

46. Klohs J, Deistung A, Schweser F, et al. Detection of cerebral microbleeds with quantitative susceptibility mapping in the ArcAbeta mouse model of cerebral

amyloidosis. J Cereb Blood Flow Metab 2011;31(12):2282-2292.

47. Chung KK, Anderson NE, Hutchinson D, Synek B, Barber PA. Cerebral amyloid angiopathy related inflammation: three case reports and a review. J Neurol Neurosurg Psychiatry 2011;82(1):20-26.

48. Kikuta K, Takagi Y, Nozaki K, et al. Early experience with 3-T magnetic resonance tractography in the surgery of cerebral arteriovenous malformations in and around the visual pathway. Neurosurgery 2006;58(2):331-337; discussion 331-337.

49. Fujimura M, Tominaga T, Kuroda S, et al. 2021 Japanese Guidelines for the Management of Moyamoya Disease: Guidelines from the Research Committee on Moyamoya Disease and Japan Stroke Society. Neurol Med Chir (Tokyo) 2022;62(4):165-170.

50. Mori N, Miki Y, Kikuta K, et al. Microbleeds in moyamoya disease: susceptibility-weighted imaging versus T2*-weighted imaging at 3 Tesla. Invest Radiol 2008;43(8):574-579.

51. Oshima S, Fushimi Y, Okada T, et al. Neuromelanin-Sensitive Magnetic Resonance Imaging Using DANTE Pulse. Mov Disord 2021;36(4):874-882.

52. Furukawa K, Shima A, Kambe D, et al. Motor Progression and Nigrostriatal

Neurodegeneration in Parkinson Disease. Ann Neurol 2022;92(1):110-121.

53. He N, Chen Y, LeWitt PA, Yan F, Haacke EM. Application of Neuromelanin MR Imaging in Parkinson Disease. J Magn Reson Imaging 2023;57(2):337-352.

54. Du G, Liu T, Lewis MM, et al. Quantitative susceptibility mapping of the midbrain in Parkinson's disease. Mov Disord 2016;31(3):317-324.

55. Biondetti E, Santin MD, Valabregue R, et al. The spatiotemporal changes in dopamine, neuromelanin and iron characterizing Parkinson's disease. Brain 2021;144(10):3114-3125.

56. Vroegindeweij LHP, Bossoni L, Boon AJW, et al. Quantification of different iron forms in the aceruloplasminemia brain to explore iron-related neurodegeneration. Neuroimage Clin 2021;30:102657.

57. Zeng J, Xing W, Liao W, Wang X. Magnetic resonance imaging, susceptibility weighted imaging and quantitative susceptibility mapping findings of pantothenate kinase-associated neurodegeneration. J Clin Neurosci 2019;59:20-28.

58. Dusek P, Mekle R, Skowronska M, et al. Brain iron and metabolic abnormalities in C19orf12 mutation carriers: A 7.0 tesla MRI study in mitochondrial membrane protein-associated neurodegeneration. Mov Disord 2020;35(1):142-150.

59. Bhattarai A, Egan GF, Talman P, Chua P, Chen Z. Magnetic Resonance Iron Imaging in Amyotrophic Lateral Sclerosis. J Magn Reson Imaging 2022;55(5):1283-1300.

60. Schweitzer AD, Liu T, Gupta A, et al. Quantitative susceptibility mapping of the motor cortex in amyotrophic lateral sclerosis and primary lateral sclerosis. AJR Am J Roentgenol 2015;204(5):1086-1092.

61. Conte G, Contarino VE, Casale S, et al. Amyotrophic lateral sclerosis phenotypes significantly differ in terms of magnetic susceptibility properties of the precentral cortex. Eur Radiol 2021;31(7):5272-5280.

62. Acosta-Cabronero J, Machts J, Schreiber S, et al. Quantitative Susceptibility MRI to Detect Brain Iron in Amyotrophic Lateral Sclerosis. Radiology 2018;289(1):195-203.

63. Sugiyama A, Sato N, Kimura Y, et al. Quantifying iron deposition in the cerebellar subtype of multiple system atrophy and spinocerebellar ataxia type 6 by quantitative susceptibility mapping. J Neurol Sci 2019;407:116525.

64. Deistung A, Jaschke D, Draganova R, et al. Quantitative susceptibility mapping reveals alterations of dentate nuclei in common types of degenerative cerebellar ataxias. Brain Commun 2022;4(1):fcab306.

65. Ferro A, Sheeler C, Rosa JG, Cvetanovic M. Role of Microglia in Ataxias. J Mol Biol 2019;431(9):1792-1804.

66. Sasaki H, Kojima H, Yabe I, et al. Neuropathological and molecular studies of spinocerebellar ataxia type 6 (SCA6). Acta Neuropathol 1998;95(2):199-204.

67. Tikka S, Baumann M, Siitonen M, et al. CADASIL and CARASIL. Brain Pathol 2014;24(5):525-544.

68. Hong H, Wang S, Yu X, et al. White Matter Tract Injury by MRI in CADASIL Patients is Associated With Iron Accumulation. J Magn Reson Imaging 2023;57(1):238-245.

69. van Rooden S, Versluis MJ, Liem MK, et al. Cortical phase changes in Alzheimer's disease at 7T MRI: a novel imaging marker. Alzheimers Dement 2014;10(1):e19-26.

70. van Bergen JM, Li X, Hua J, et al. Colocalization of cerebral iron with Amyloid beta in Mild Cognitive Impairment. Sci Rep 2016;6:35514.

71. Yamaguchi A, Kudo K, Sato R, et al. Efficacy of Quantitative Susceptibility Mapping with Brain Surface Correction and Vein Removal for Detecting Increase Magnetic Susceptibility in Patients with Alzheimer's Disease. Magn Reson Med Sci 2023;22(1):87-94.

72. Ayton S, Faux NG, Bush AI, Alzheimer's Disease Neuroimaging I. Ferritin levels in the cerebrospinal fluid predict Alzheimer's disease outcomes and are regulated by APOE. Nat Commun 2015;6:6760.

73. van Rooden S, Doan NT, Versluis MJ, et al. 7T T(2)*-weighted magnetic resonance imaging reveals cortical phase differences between early- and late-onset Alzheimer's disease. Neurobiol Aging 2015;36(1):20-26.

74. Sato R, Kudo K, Udo N, et al. A diagnostic index based on quantitative susceptibility mapping and voxel-based morphometry may improve early diagnosis of Alzheimer's disease. Eur Radiol 2022;32(7):4479-4488.

75. Peters MEM, de Brouwer EJM, Bartstra JW, et al. Mechanisms of calcification in Fahr disease and exposure of potential therapeutic targets. Neurol Clin Pract 2020;10(5):449-457.

76. Ukai K, Kosaka K. Diffuse neurofibrillary tangles with calcification (Kosaka-Shibayama disease) in Japan. Psychiatry Clin Neurosci 2016;70(3):131-140.

77. Hattingen E, Beyle A, Muller A, Klockgether T, Kornblum C. Wernicke encephalopathy: SWI detects petechial hemorrhages in mammillary bodies in vivo. Neurology 2016;87(18):1956-1957.

78. Nakamura Y, Fushimi Y, Hinoda T, et al. Hemosiderin Detection inside the

Mammillary Bodies Using Quantitative Susceptibility Mapping on Patients with Wernicke-Korsakoff Syndrome. Magn Reson Med Sci 2022:in press. doi: 10.2463/mrms.ici.2022-0109.

79. Wijdicks EFM. Hepatic Encephalopathy. New England Journal of Medicine 2016;375(17):1660-1670.

80. Klos KJ, Ahlskog JE, Kumar N, et al. Brain metal concentrations in chronic liver failure patients with pallidal T1 MRI hyperintensity. Neurology 2006;67(11):1984-1989.

81. Young RJ, Knopp EA. Brain MRI: tumor evaluation. J Magn Reson Imaging 2006;24(4):709-724.

82. Tanji M, Mineharu Y, Sakata A, et al. High intratumoral susceptibility signal grade on susceptibility-weighted imaging: a risk factor for hemorrhage after stereotactic biopsy. J Neurosurg 2023;138(1):120-127.

83. Tsukamoto T, Miki Y. Imaging of pituitary tumors: an update with the 5th WHO Classifications-part 2. Neoplasms other than PitNET and tumor-mimicking lesions. Jpn J Radiol 2023.

84. Kakigi T, Okada T, Kanagaki M, et al. Quantitative imaging values of CT, MR, and FDG-PET to differentiate pineal parenchymal tumors and germinomas: are

they useful? Neuroradiology 2014;56(4):297-303.

85. Nakasu S, Fukami T, Nakajima M, Watanabe K, Ichikawa M, Matsuda M. Growth pattern changes of meningiomas: long-term analysis. Neurosurgery 2005;56(5):946-955; discussion 946-955.

86. Aiken AH, Akgun H, Tihan T, Barbaro N, Glastonbury C. Calcifying pseudoneoplasms of the neuraxis: CT, MR imaging, and histologic features. AJNR Am J Neuroradiol 2009;30(6):1256-1260.

87. Bähr O, Hattingen E, Rieger J, Steinbach JP. Bevacizumab-induced tumor calcifications as a surrogate marker of outcome in patients with glioblastoma. Neuro Oncol 2011;13(9):1020-1029.

88. Remes TM, Suo-Palosaari MH, Koskenkorva PKT, et al. Radiation-induced accelerated aging of the brain vasculature in young adult survivors of childhood brain tumors. Neurooncol Pract 2020;7(4):415-427.

89. Metoki T, Mugikura S, Higano S, et al. Subcortical calcification on CT in dural arteriovenous fistula with cortical venous reflux. AJNR Am J Neuroradiol 2006;27(5):1076-1078.

90. Yang MS, Chen CC, Cheng YY, Yeh DM, Lee SK, Tyan YS. Unilateral subcortical calcification: a manifestation of dural arteriovenous fistula. AJNR Am J

Neuroradiol 2005;26(5):1149-1151.

91. Stapleton CJ, Barker FG, 2nd. Cranial Cavernous Malformations: Natural History and Treatment. Stroke 2018;49(4):1029-1035.

92. Tan H, Liu T, Wu Y, et al. Evaluation of iron content in human cerebral cavernous malformation using quantitative susceptibility mapping. Invest Radiol 2014;49(7):498-504.

93. Perez-Malagon CD, Barrera-Rodriguez R, Lopez-Gonzalez MA, Alva-Lopez LF. Diagnostic and Neurological Overview of Brain Tuberculomas: A Review of Literature. Cureus 2021;13(12):e20133.

94. Benson JC, Cervantes G, Baron TR, et al. Imaging features of neurotoxoplasmosis: A multiparametric approach, with emphasis on susceptibility-weighted imaging. Eur J Radiol Open 2018;5:45-51.

95. Kanda T, Ishii K, Kawaguchi H, Kitajima K, Takenaka D. High signal intensity in the dentate nucleus and globus pallidus on unenhanced T1-weighted MR images: relationship with increasing cumulative dose of a gadolinium-based contrast material. Radiology 2014;270(3):834-841.

96. Nakamichi R, Taoka T, Kawai H, Yoshida T, Sone M, Naganawa S. Magnetic resonance cisternography imaging findings related to the leakage of Gadolinium

into the subarachnoid space. Jpn J Radiol 2021;39(10):927-937.

97. Hinoda T, Fushimi Y, Okada T, et al. Quantitative assessment of gadolinium deposition in dentate nucleus using quantitative susceptibility mapping. J Magn Reson Imaging 2017;45(5):1352-1358.

98. Choi Y, Jang J, Kim J, et al. MRI and Quantitative Magnetic Susceptibility Maps of the Brain after Serial Administration of Gadobutrol: A Longitudinal Follow-up Study. Radiology 2020;297(1):143-150.

99. Frenzel T, Lengsfeld P, Schirmer H, Hutter J, Weinmann HJ. Stability of gadolinium-based magnetic resonance imaging contrast agents in human serum at 37 degrees C. Invest Radiol 2008;43(12):817-828.

100. Remacha A, Sanz C, Contreras E, et al. Guidelines on haemovigilance of post-transfusional iron overload. Blood Transfus 2013;11(1):128-139.

101. Hasiloglu ZI, Asik M, Ure E, Ertem F, Apak H, Albayram S. The utility of susceptibility-weighted imaging to evaluate the extent of iron accumulation in the choroid plexus of patients with beta-thalassaemia major. Clin Radiol 2017;72(10):903 e901-903 e907.

102. Manara R, Ponticorvo S, Tartaglione I, et al. Brain iron content in systemic iron overload: A beta-thalassemia quantitative MRI study. Neuroimage Clin

2019;24:102058.

103. Dimov AV, Li J, Nguyen TD, et al. QSM Throughout the Body. J Magn Reson Imaging 2023;57(6):1621-1640.

104. Fushimi Y, Yoshida K, Okawa M, et al. Vessel wall MR imaging in neuroradiology. Radiol Med 2022;127(9):1032-1045.

105. Wang C, Zhang Y, Du J, et al. Quantitative Susceptibility Mapping for Characterization of Intraplaque Hemorrhage and Calcification in Carotid Atherosclerotic Disease. J Magn Reson Imaging 2020;52(2):534-541.

106. Ikebe Y, Ishimaru H, Imai H, et al. Quantitative Susceptibility Mapping for Carotid Atherosclerotic Plaques: A Pilot Study. Magn Reson Med Sci 2020;19(2):135-140.

107. Stone AJ, Tornifoglio B, Johnston RD, Shmueli K, Kerskens C, Lally C. Quantitative susceptibility mapping of carotid arterial tissue ex vivo: Assessing sensitivity to vessel microstructural composition. Magn Reson Med 2021;86(5):2512-2527.

108. Sharma SD, Hernando D, Horng DE, Reeder SB. Quantitative susceptibility mapping in the abdomen as an imaging biomarker of hepatic iron overload. Magn Reson Med 2015;74(3):673-683.

109. Tipirneni-Sajja A, Loeffler RB, Hankins JS, Morin C, Hillenbrand CM. Quantitative Susceptibility Mapping Using a Multispectral Autoregressive Moving Average Model to Assess Hepatic Iron Overload. J Magn Reson Imaging 2021;54(3):721-727.

110. Yokoo T, Browning JD. Fat and iron quantification in the liver: past, present, and future. Top Magn Reson Imaging 2014;23(2):73-94.

111. Albano D, Bruno F, Agostini A, et al. Dynamic contrast-enhanced (DCE) imaging: state of the art and applications in whole-body imaging. Jpn J Radiol 2022;40(4):341-366.

112. Straub S, Laun FB, Emmerich J, et al. Potential of quantitative susceptibility mapping for detection of prostatic calcifications. J Magn Reson Imaging 2017;45(3):889-898.

Figure legends

Figure 1

A female baby born weighting 2100g. QSM obtained at a corrected age of 38 weeks shows no apparent paramagnetic regions in the basal ganglia (white arrows) (a). Bilateral basal veins and internal cerebral veins (gray arrows) show positive susceptibility (a, b).

On follow-up MR imaging was obtained at the age of 2 years 11months, QSM shows positive susceptibility in the basal ganglia (white arrows) (c), and negative susceptibility in white matter such as the internal capsule (black arrowheads). Bilateral basal veins and internal cerebral veins (gray arrows) also show positive susceptibility (c, d).

Figure 2

A 64-year-old woman who underwent brain CT (a) and MR imaging (b) due to mild headache. CT shows high attenuation spots (black arrows) in the medial part of the globus pallidus representing calcification, while QSM shows positive susceptibility suggesting mineralization (black arrows). Such “paradoxical calcification” is explained by the high attenuation of calcification in the vessel walls on CT and the positive susceptibility associated with iron present in the vessel wall overwhelming diamagnetic components such as calcification on QSM. Note that CT shows high attenuation and QSM shows negative susceptibility in the pineal body suggesting physiological calcification of the pineal body (white arrow).

Figure 3

A 65-year old man. T2WI shows hyperintensity in the subcortical white matter of bilateral

frontal lobes with left side predominance (black arrowheads) (a). SWI shows multiple punctate hypointense spots in the cerebral cortex where T2WI shows hyperintensity (white arrows) (b). QSM shows positive susceptibility representing hemosiderin associated with cerebral amyloid angiopathy (black arrows) (c). Cerebral amyloid angiopathy (CAA)-related inflammation was diagnosed after brain biopsy. After steroid therapy, abnormal white matter intensity improved.

Figure4

A 30-year-old woman with moyamoya disease. Time-of-flight (TOF) MRA shows an abnormally dilated collateral artery along the right lateral ventricle (arrow), forming a peripheral aneurysm (a). SWI shows low intensity around the aneurysm (arrow) (b) and QSM shows positive susceptibility suggestive of microhemorrhage around the peripheral aneurysm (arrow) (c). The aneurysm was also confirmed on conventional angiography (arrow) (d).

Figure 5

A 76-year-old man with hypertension and dyslipidemia. Non-enhanced CT shows areas of very high attenuation in the cerebellum (black arrows), but brain CT in the bone

window shows speckled high attenuation areas (black arrows) (b). T1WI shows high intensity areas corresponding to regions of high attenuation on CT (black arrows) (c). T1WI also shows low intensity areas in bilateral dentate nuclei (white arrows) (c). QSM shows negative susceptibility values representing calcification (black arrows) and areas of increased positive susceptibility in the dentate nuclei (white arrows) (d).

Figure 6

SWI and QSM in a 55-year-old man with Wernicke encephalopathy (a, d), a 52-year-old man with Wernicke encephalopathy (b, e), and a 55-year-old man with dizziness and no intracranial lesions as a control patient (c, f). SWI shows low-intensity spots in both mammillary bodies in patients with Wernicke encephalopathy (a, b), corresponding to positive susceptibility in QSM (d, e). Conversely, SWI shows no abnormal signal in the mammillary bodies (c), and QSM shows no apparent positive susceptibility. White arrows indicate mammillary bodies. This figure is reprinted with permission from the authors of Reference (78).

Figure 7

A 60-year-old man with hepatic encephalopathy associated with metastatic hepatic

tumors. CT shows no major abnormalities (a). T1WI shows hyperintense areas in bilaterally in the globus pallidus (black arrows) (b). SWI shows punctate low intensity spots in the globus pallidus (black arrows) and choroid plexus (white arrows) (c). QSM shows punctate positive susceptibility suggesting mineralization (black arrows) and spots of negative susceptibility bilaterally in the choroid plexus suggesting physiological calcification (white arrows).

Figure 8

A 75-year-old woman diagnosed with glioblastoma with CSF dissemination. NE-T1WI (a) and CE-T1WI (b) show multiple enhanced nodules around the ventricle (arrows). SWI shows low intensities in some nodules (arrows) (c). QSM shows positive susceptibilities suggesting hemosiderin associated with intratumoral hemorrhage (arrows) (d).

Figure 9

A 47-year-old man with epilepsy. CT shows a high attenuation tumor in the right frontal lobe, extending to the contralateral hemisphere via the corpus callosum (a). Non-enhanced T1WI shows high signal in a small area compared with the region of high attenuation on CT (b). SWI shows a low intensity lesion relatively similar to the findings

on CT (c). QSM reveals negative susceptibility lesions suggesting calcification inside the tumor, but positive susceptibility suggesting hemosiderin at tumor periphery (d). Low-grade glioma was suspected based on the longstanding nature of the lesions. Surgery was not performed because the disease was stable, and oligodendroglioma was suspected clinically.

Figure 10

A 29-year-old man with recurrent anaplastic oligodendroglioma. FLAIR shows hyperintense area in the left temporal lobe. FLAIR also shows a small low intensity spot (arrow) (a). T1WI shows no apparent hyperintensity in the tumor (b). Non-enhanced CT shows high attenuation spots (arrow) (c). QSM shows spots of negative susceptibility corresponding to the high attenuation spots on CT, suggesting calcification (arrows) (d). Histopathological study shows microcalcification in the specimen.

Figure 11

A 20-year-old man with hydrocephalus due to pineal tumor. T1WI show a low-intensity tumor in the pineal region (a). CE-T1WI shows good enhancement in the tumor as well as a non-enhanced lesion in the posterior part of the pineal tumor (arrow) (b). Meanwhile,

SWI shows low intensity (a), and QSM shows a negative susceptibility value suggestive of calcification (arrow) (d). Based on the growth pattern with engulfing physiological pineal calcification, this tumor was considered to represent germinoma, and pathological confirmation was subsequently obtained.

Figure 12

A 73-year-old man. No abnormal neurological findings were noted and a calcified lesion near the anterior horn of the left lateral ventricle was identified incidentally (a). This lesion shows low intensity on T1WI (b), low intensity on SWI (c), and multiple areas of punctate negative susceptibility with a small amount of positive susceptibility on QSM (d). Since no increase in size was seen, the clinical diagnosis was calcifying pseudotumor of the neuraxis (CAPNON).

Figure 13

A 1-year-old girl with pial AVF. Multiple dilated flow voids and enlarged dural sinus are shown in the left occipital lobe on T2WI (a). Feeders are shown around the left lateral ventricle on TOF-MRA (b). Coil embolization was performed for the pial AVF, and non-enhanced CT performed 9 years after treatment shows multiple areas of high attenuation

in the corticomedullary junctions (black arrows) (c). QSM shows negative susceptibility values corresponding to high attenuation areas, suggesting dystrophic calcification (black arrows) (d).

Figure 14

A 30-year-old woman, diagnosed with tuberculosis infection 8 years earlier. Due to severe headache, brain CT and MR imaging were performed, revealing multiple cerebral nodules. Brain CT shows a high-attenuation nodule in the left frontal lobe (a). This nodule appears isointense with a low-intensity rim on T1WI (b), low intensity on SWI (c), and negative susceptibility on QSM, suggesting calcification (d).

Figure 15

A 35-year-old woman after bone marrow transplantation for anaplastic anemia. Toxoplasmosis was diagnosed 10 years earlier. Follow-up NE-CT showed multiple high-attenuation spots. SWI shows low intensity lesions. Meanwhile, QSM shows negative susceptibility in some lesions suggesting calcification, and positive susceptibility in other lesions suggesting old hemorrhage in calcified lesions.

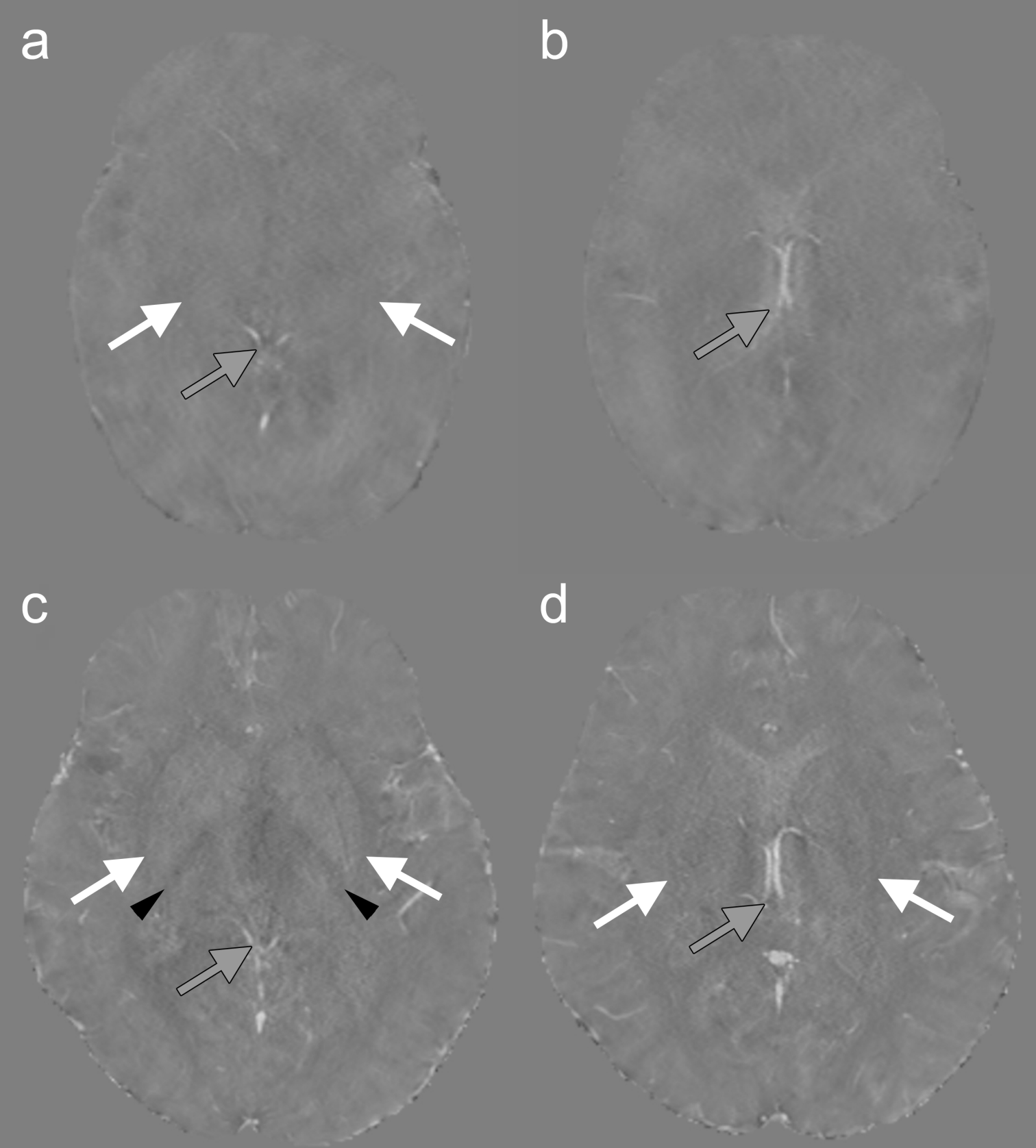
a
b
c
d

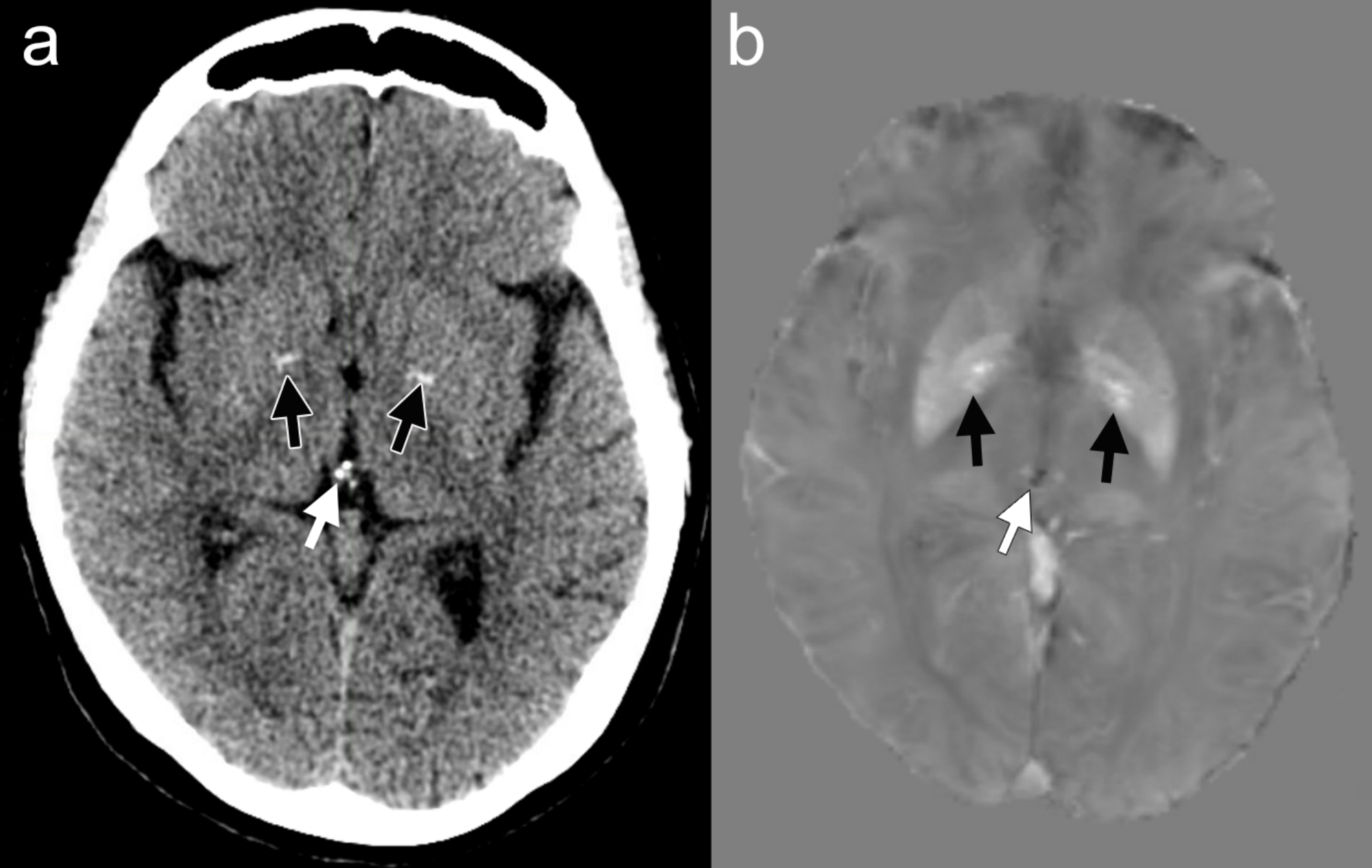
a
b

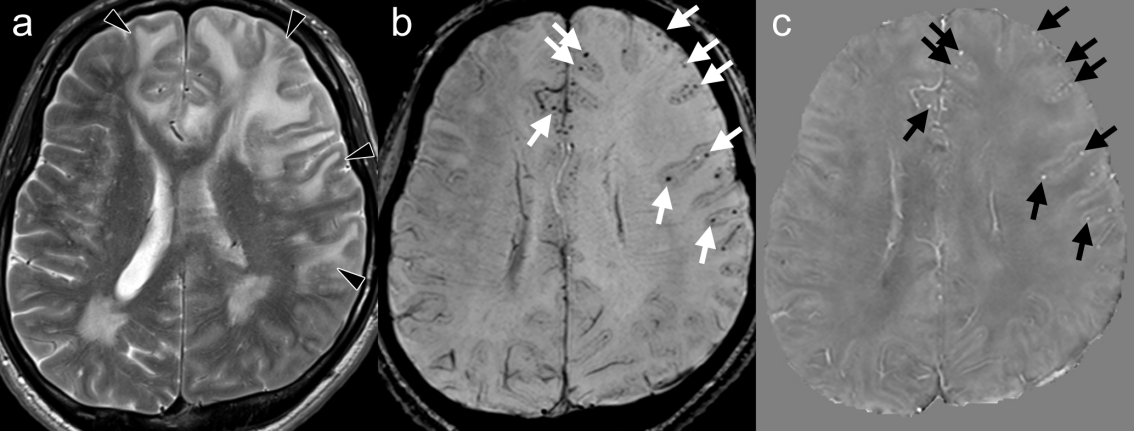
a
b
c

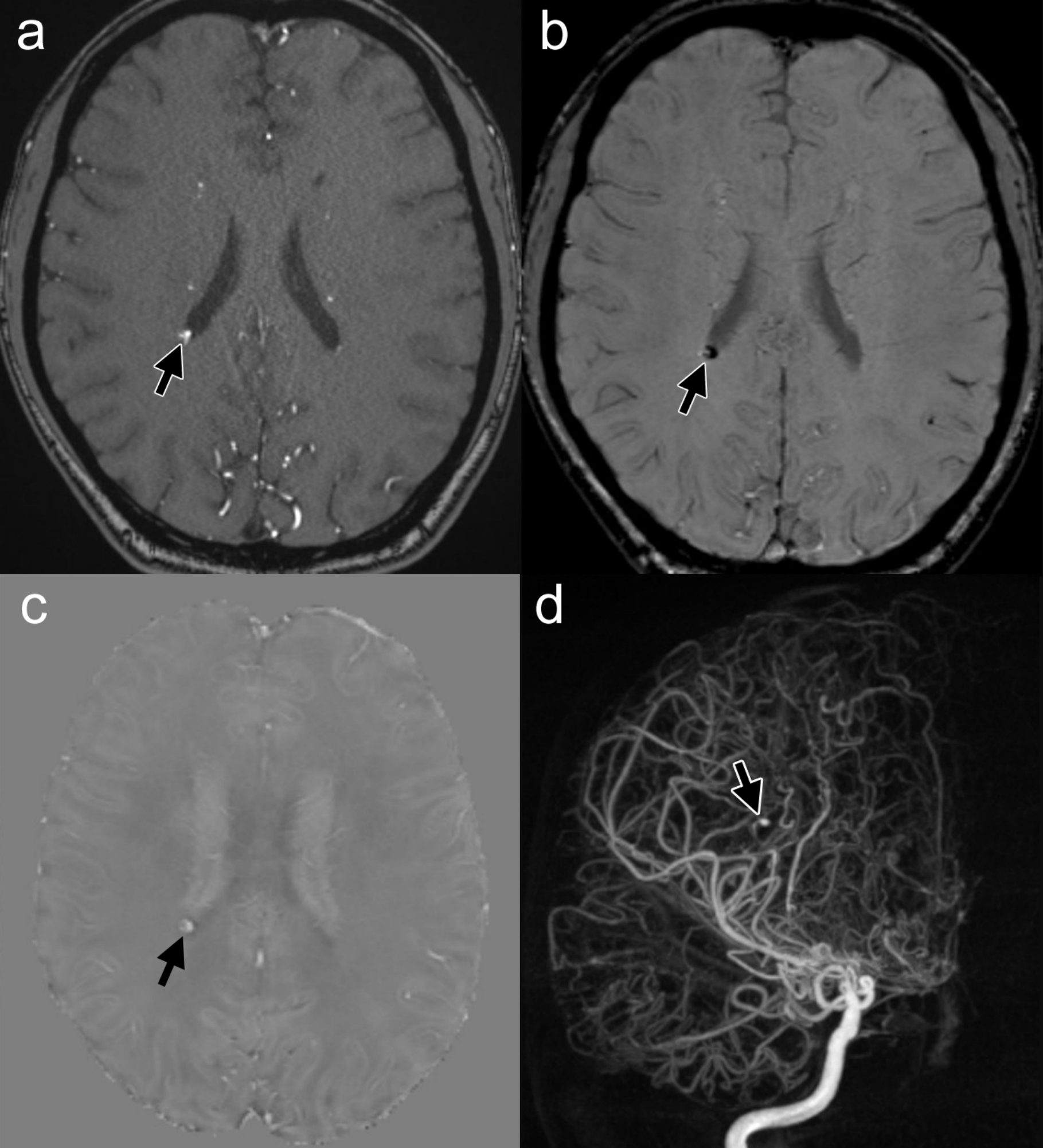
a
b
c
d

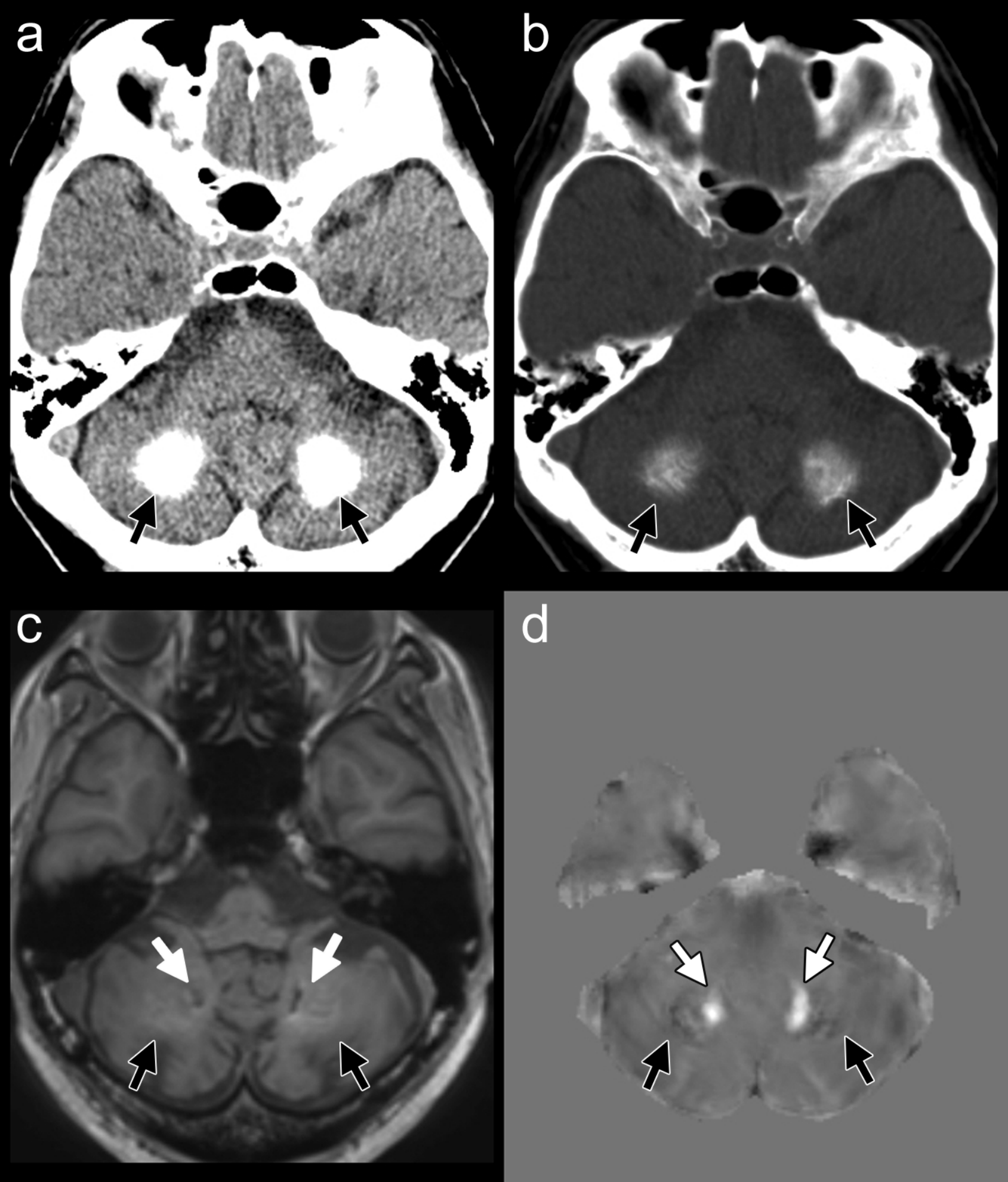
a
b
c
d

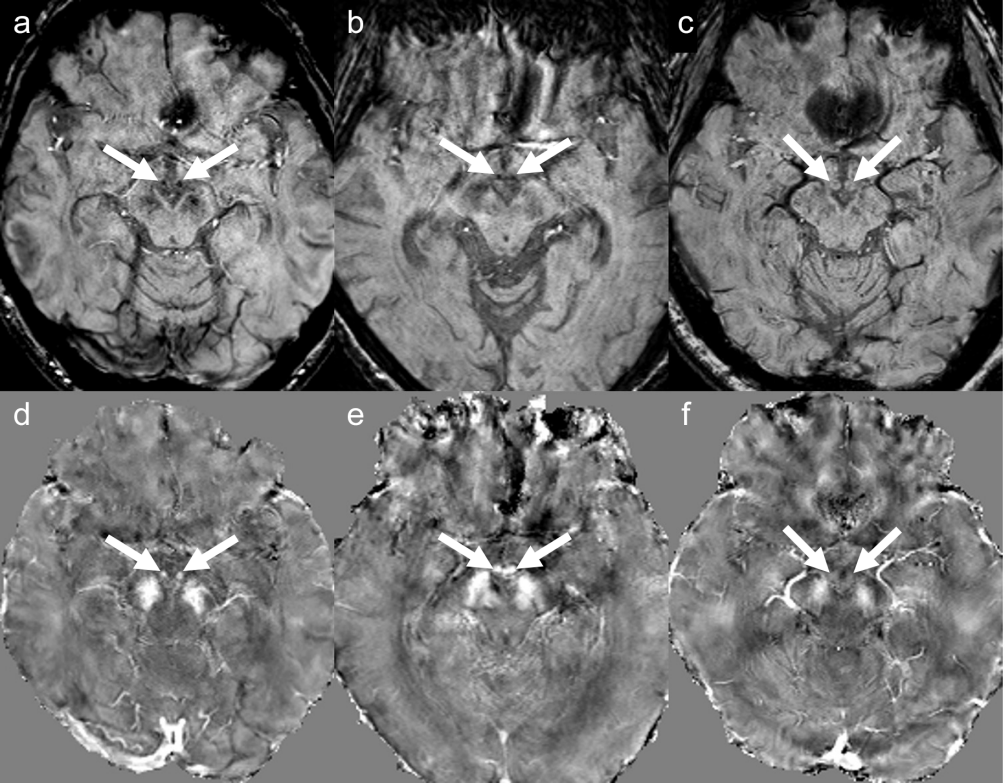
a
b
c
d
e
f
[ppm]
0.20
-0.20

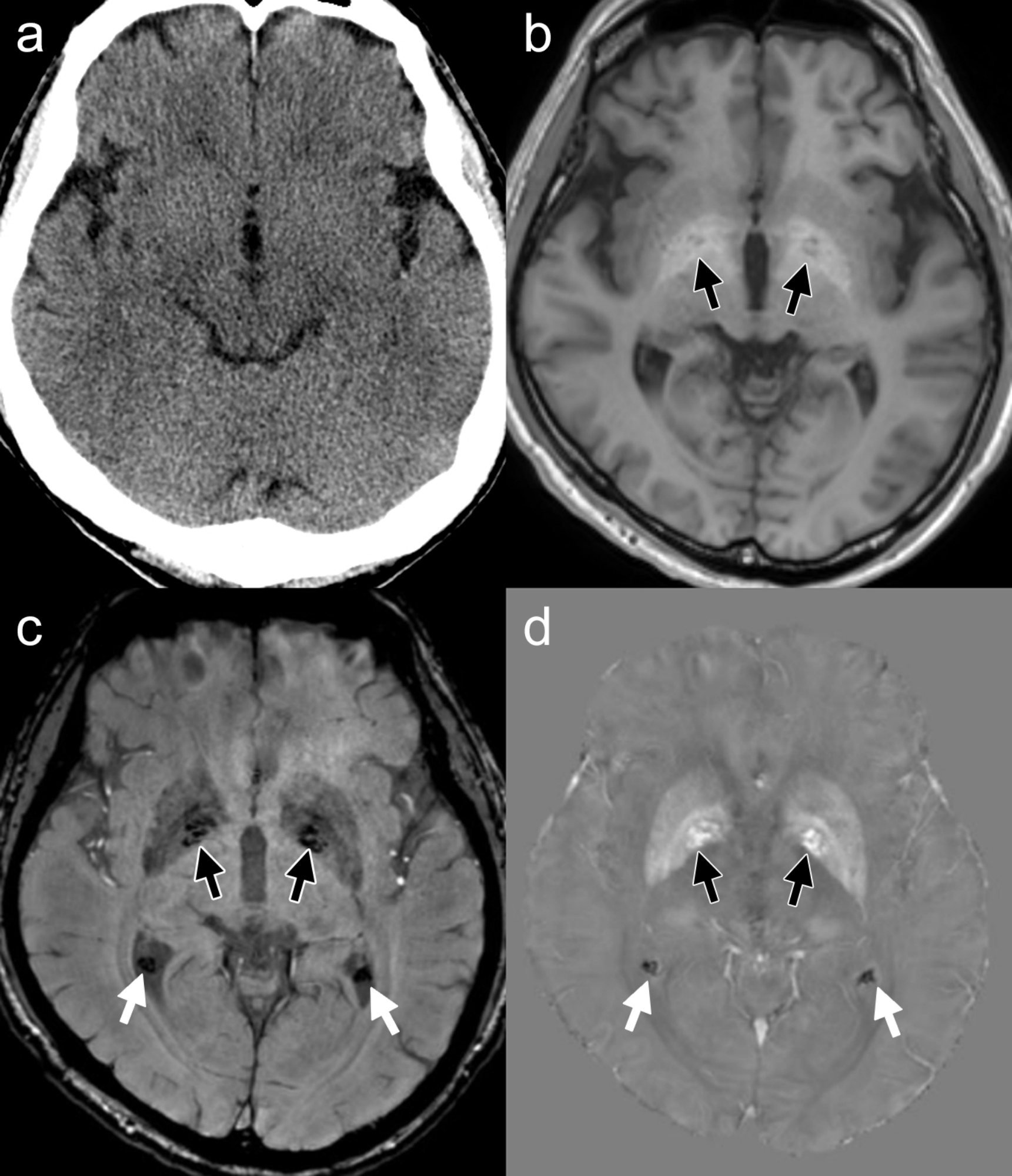
a
b
c
d

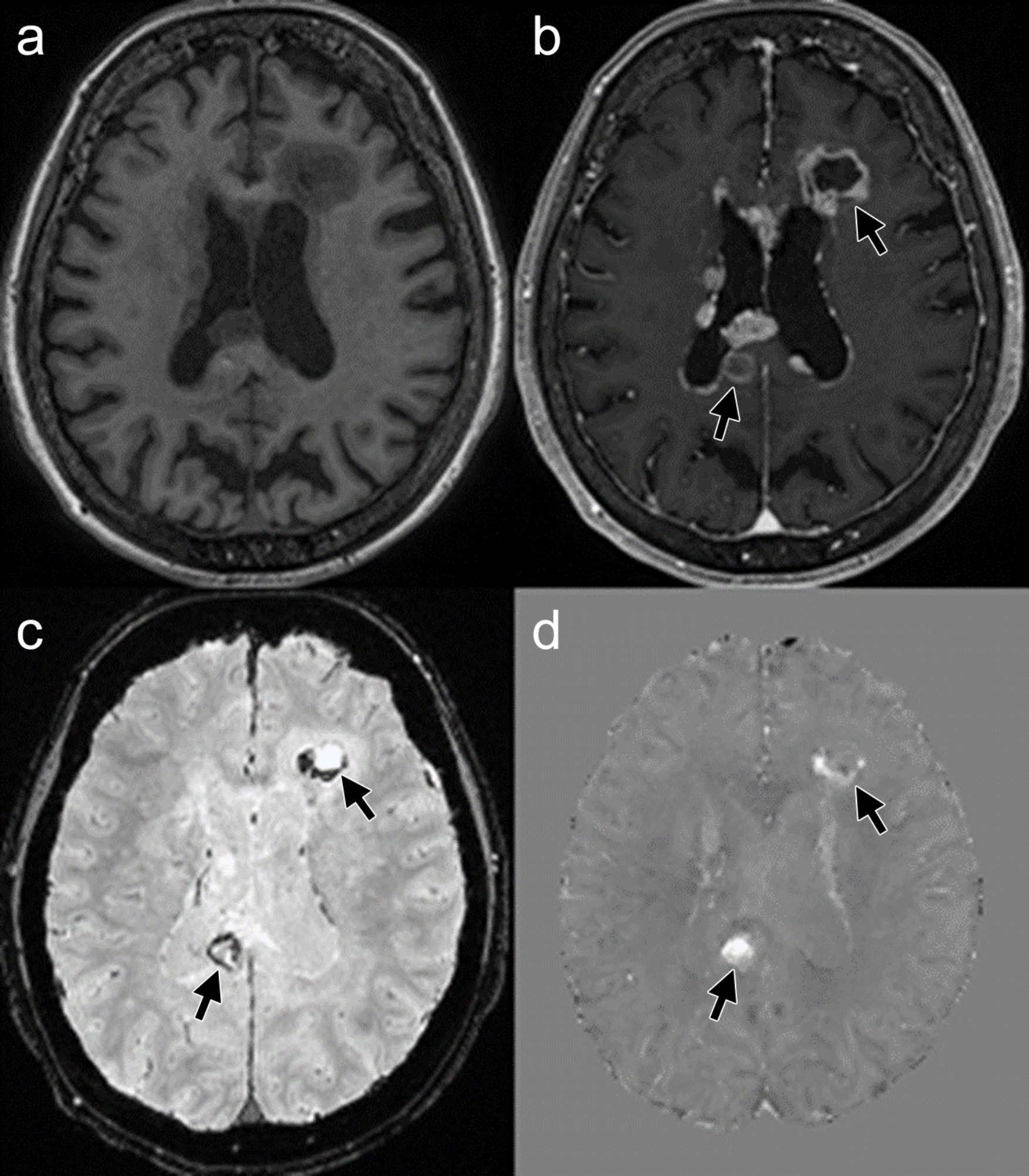
a
b
c
d

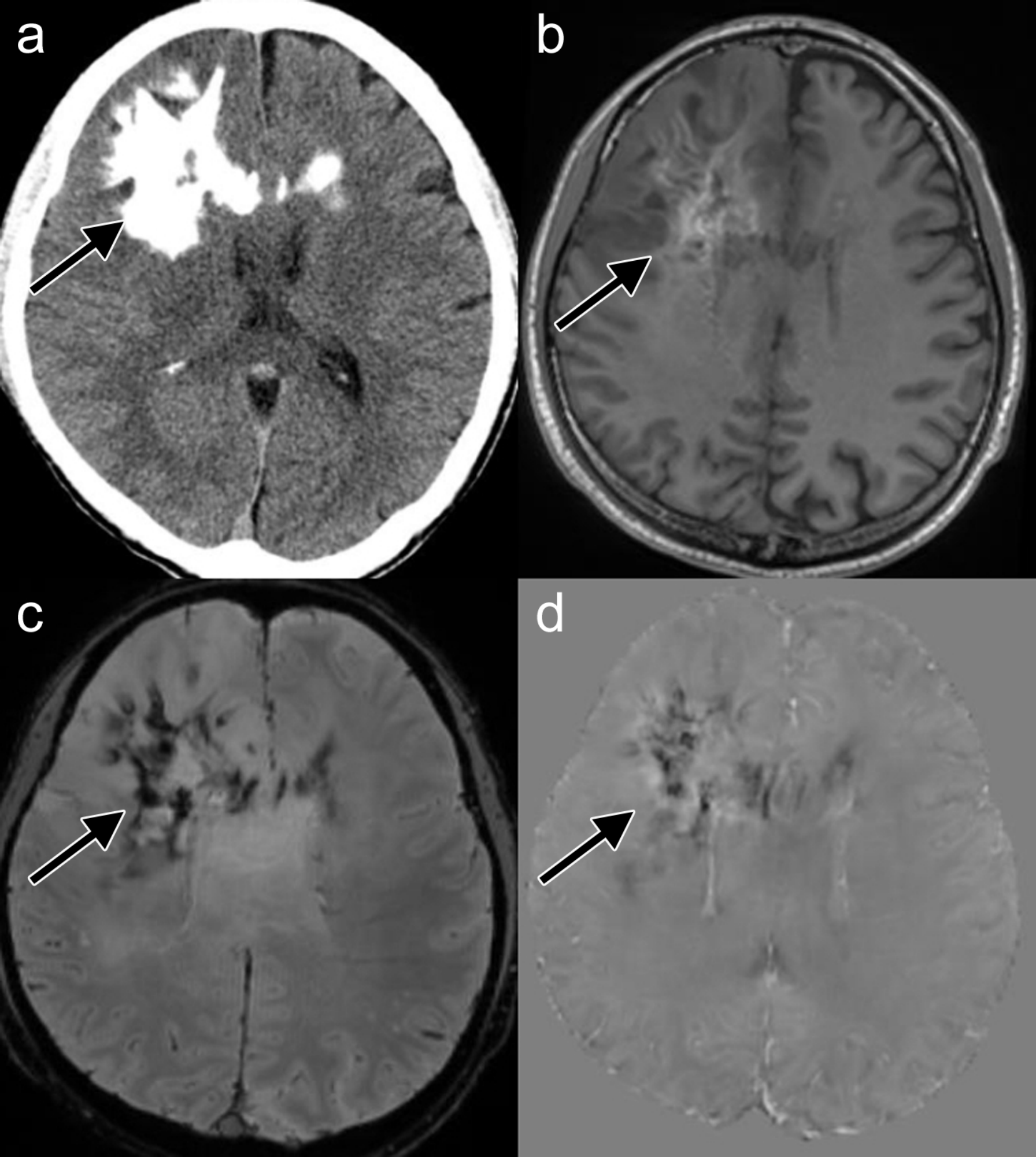
a
b
c
d

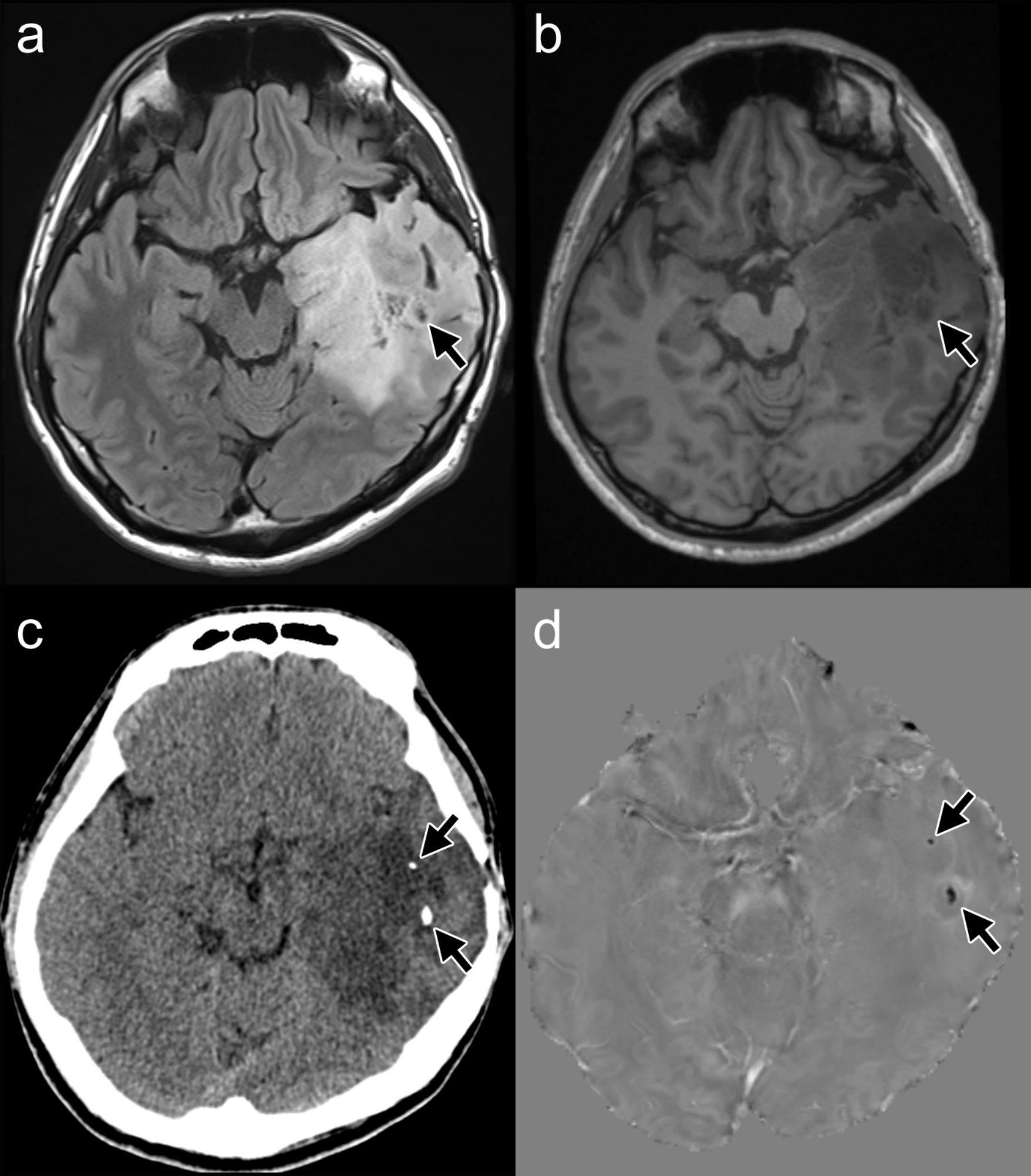
a
b
c
d

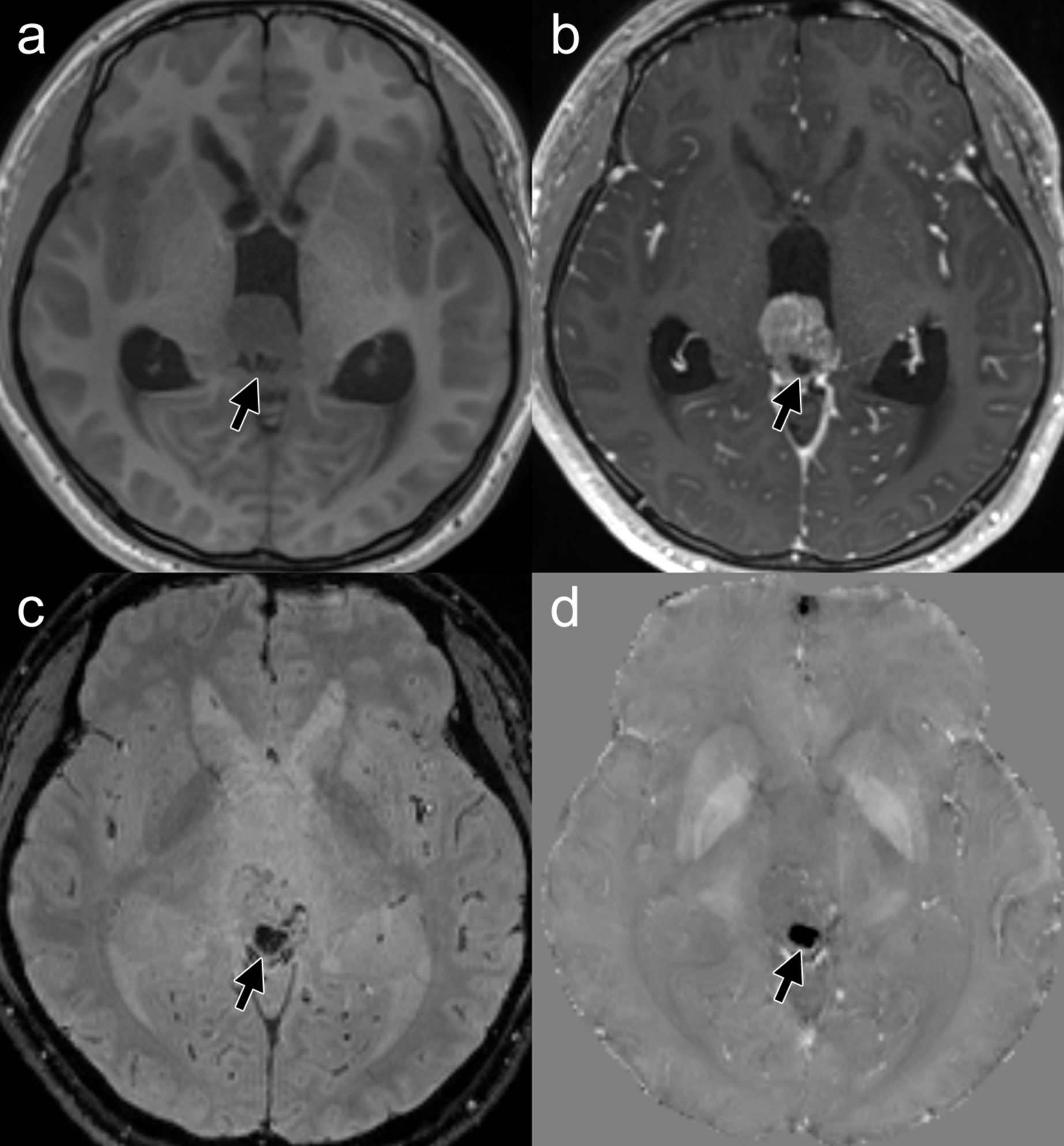
a
b
c
d

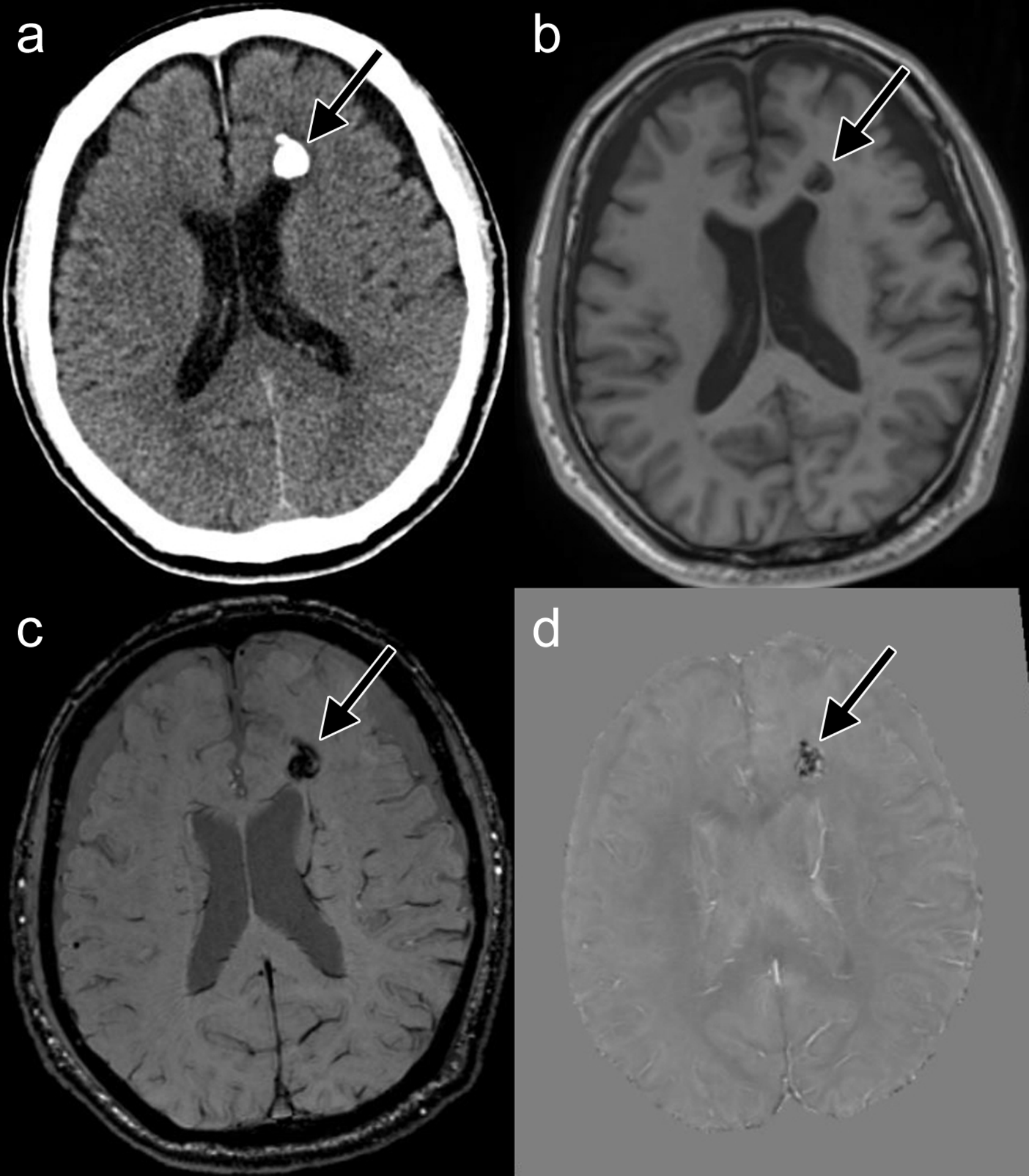
a
b
c
d

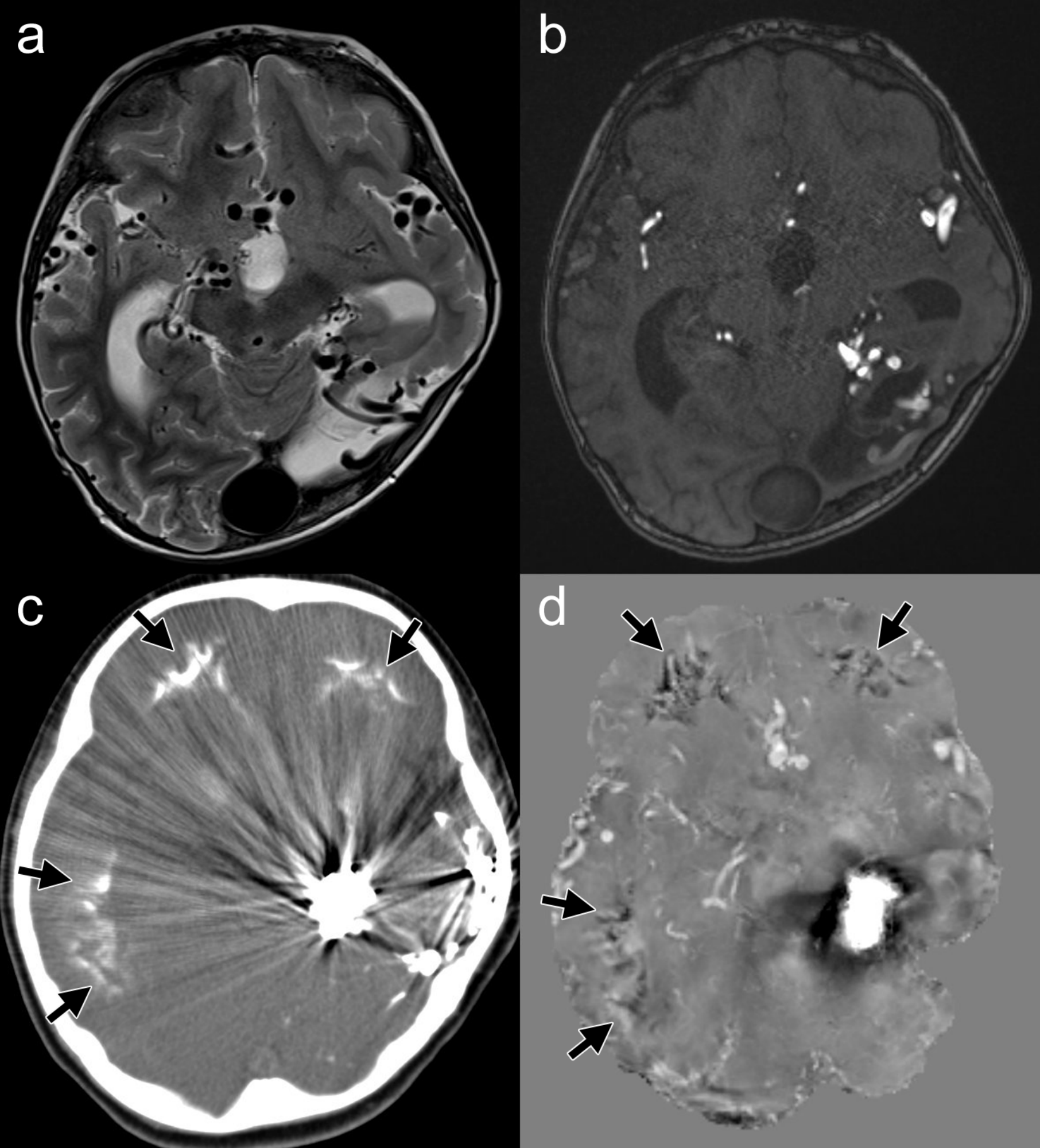
a
b
c
d

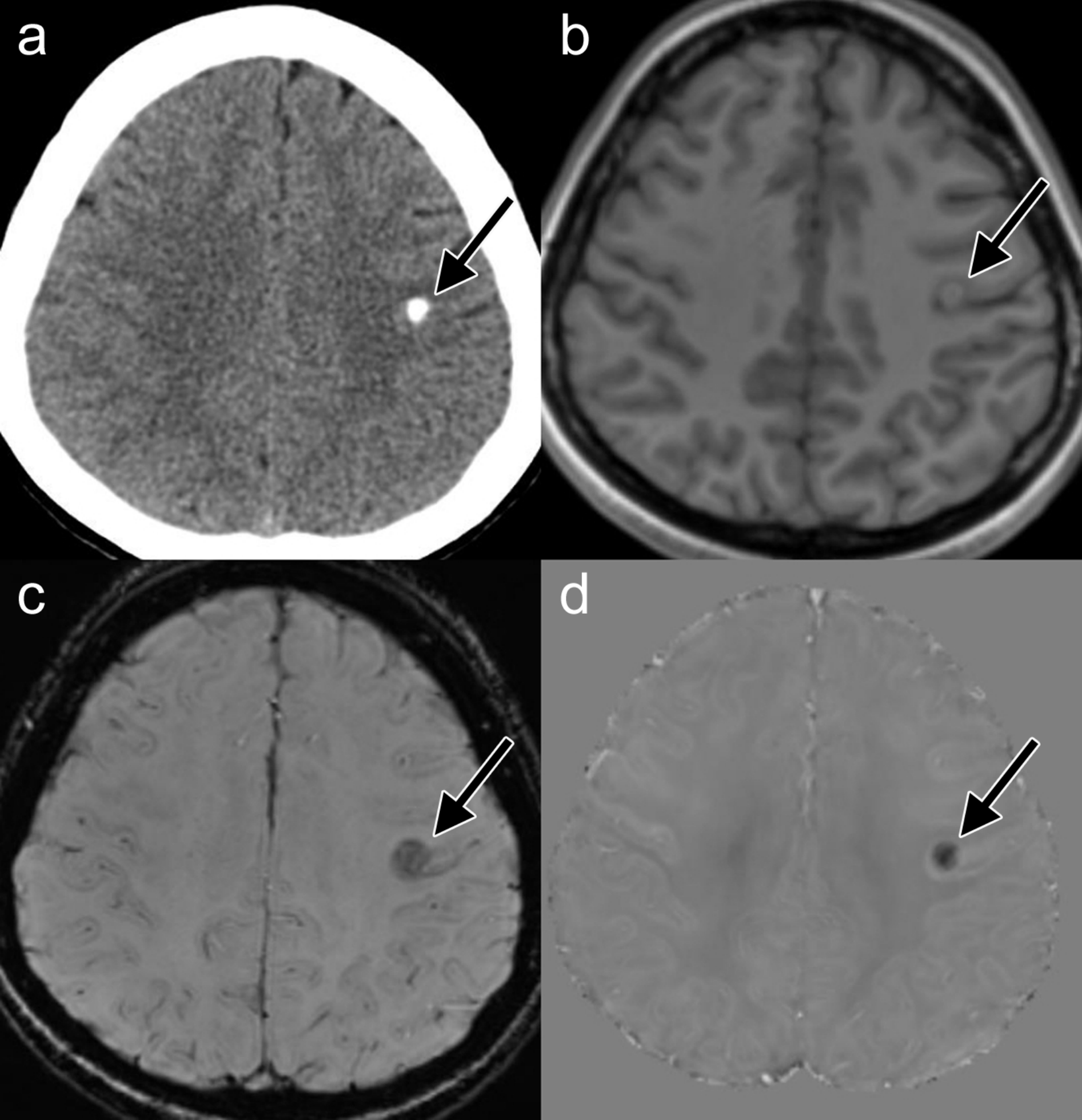
a
b
c
d

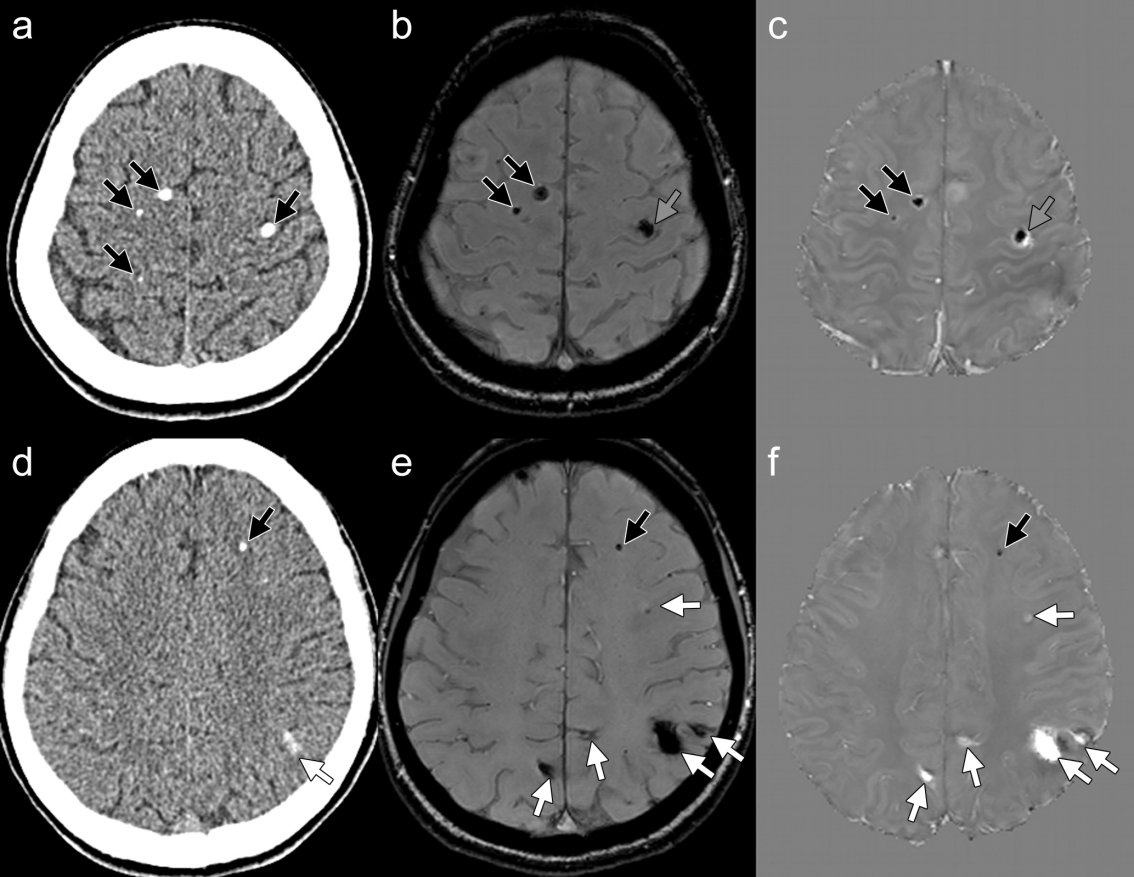
a
b
c
d
e
f